



HAL
open science

The Early Upper paleolithic deposit of Mughr el-Hamamah (Jordan): Archaeobotanical taphonomy and site formation processes

Mónica Alonso-Eguiluz, Michael Toffolo, Chantel White, Eleni Asouti, Elisabetta Boaretto, Liv Nilsson Stutz, Aaron Stutz, Rosa María Albert

► **To cite this version:**

Mónica Alonso-Eguiluz, Michael Toffolo, Chantel White, Eleni Asouti, Elisabetta Boaretto, et al.. The Early Upper paleolithic deposit of Mughr el-Hamamah (Jordan): Archaeobotanical taphonomy and site formation processes. *Journal of Archaeological Science: Reports*, 2024, 55, pp.104471. <10.1016/j.jasrep.2024.104471>. <hal-04960723>

HAL Id: hal-04960723

<https://hal.science/hal-04960723v1>

Submitted on 5 Apr 2026

HAL is a multi-disciplinary open access archive for the deposit and dissemination of scientific research documents, whether they are published or not. The documents may come from teaching and research institutions in France or abroad, or from public or private research centers.

L'archive ouverte pluridisciplinaire HAL, est destinée au dépôt et à la diffusion de documents scientifiques de niveau recherche, publiés ou non, émanant des établissements d'enseignement et de recherche français ou étrangers, des laboratoires publics ou privés.



Distributed under a Creative Commons CC BY-NC-ND 4.0 - Attribution - Non-commercial use - No Derivative Works - International License

1 **The Early Upper Paleolithic deposit of Mughr el-Hamamah (Jordan): Archaeobotanical**
2 **taphonomy and site formation processes**

3 Mónica Alonso-Eguiluz^{1,*}, Michael B. Toffolo^{2,3}, Chantel E. White⁴, Eleni Asouti⁵, Elisabetta Boaretto⁶, Liv
4 Nilsson Stutz⁷, Aaron Stutz⁸ and Rosa María Albert^{9,10}

5 ¹ Archaeology, Environmental Changes and Geo-Chemistry (AMGC). Vrije Universiteit Brussel, Belgium

6 ² Geochronology and Geology Program. Centro Nacional de Investigación sobre la Evolución Humana
7 (CENIEH), Spain

8 ³ Archéosciences Bordeaux, UMR 6034 CNRS. Université Bordeaux Montaigne, France

9 ⁴ Center for the Analysis of Archaeological Materials. University of Pennsylvania Museum of Archaeology
10 and Anthropology, United States

11 ⁵ Department of Archaeology, Classics and Egyptology. University of Liverpool, United Kingdom

12 ⁶ Scientific Archaeological Unit, Kimmel Center for Archaeological Science. Weizmann Institute of
13 Science, Israel

14 ⁷ Department of Cultural Sciences. Linnaeus University, Sweden

15 ⁸ Bohusläns Museum, Sweden

16 ⁹ Department of Prehistory. Autonomous University of Barcelona, Spain

17 ¹⁰ ICREA, Pg. Lluís Companys, 23, Barcelona, Spain

18 *Corresponding author: monica.alonso.eguiluz@vub.be

19 Department of Art Studies and Archaeology

20 Faculty of Arts and Philosophy

21 Building C - Room 5.22

22 Pleinlaan 2

23 1050 Brussel

24 Belgium

25

26 **ABSTRACT**

27 With a rich, well-dated Early Upper Palaeolithic layer, the Mughr el-Hamamah cave site is key
28 for understanding the Middle-Upper Palaeolithic transition in the Levant. The archaeological
29 deposit consists of two units. Layer A resulted from pastoral activities during the 20th century
30 and Layer B dated between 44.5-40.0 ky BP. During Layer A's formation, shepherds disturbed
31 Layer B, redepositing Early Upper Palaeolithic sediments and lithic artefacts in Layer A matrix.
32 Activity from Layer A's formation also resulted in spatially patchy percolation and bioturbation,
33 leaving microarchaeological traces such as dung spherulites in some areas in Layer B. In
34 contrast, contemporaneous chemical diagenetic processes from Layer B's primary formation
35 caused spatially uneven post-depositional dissolution of animal bone. In this article we present
36 a multi-proxy microarchaeological approach to investigate the post-depositional processes in
37 Layer B, focussing on possible impacts on the plant archaeological record. The identification of
38 intrusive spherulites from shepherds' activities define the limits of disturbance in Layer B.
39 Micromorphological analyses have identified four intact micro-facies in Layer B, representing
40 an interplay of natural and anthropogenic factors. Micromorphological details in bedded
41 combustion features favour the interpretation that associated phytoliths represent fuel traces.
42 Dicot fruit phytoliths occur in the western area of the cave, where well-preserved charred
43 wood and seeds were also found. Grass-diagnostic phytoliths correspond to C₃ and C₄ taxa,
44 indicating an overall humid environment with dry spells. Microarchaeological analysis identifies
45 traces of both bedded and dispersed hearth materials, mixed with variable plant resources for

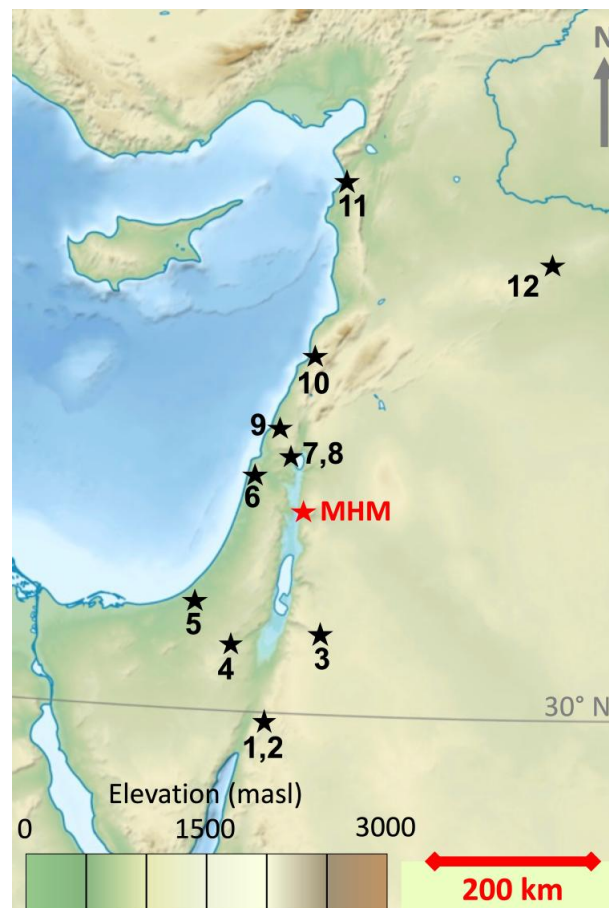
46 food, fuel, and possibly other uses. This strengthens the interpretation of Mughr el-Hamamah
47 Layer B as a dense, complicated palimpsest of recurring activities, formed over many millennia.

48

49 **keywords:** Early Upper Palaeolithic; Post-depositional processes; Micromorphology; Phytoliths;
50 FTIR; Spherulites; Cave archaeology

51 1. Introduction

52 Mughr el-Hamamah (hereafter MHM) is located in the Ajlun Governorate (Jordan) (Fig. 1), in an
53 ecotone between the wetland and steppe vegetation of Lake Lisan and the Mediterranean
54 forest of the Jordanian plateau (Stutz and Nilsson Stutz, 2017). The main cave preserves an
55 archaeological deposit with unconformably superposed layers A and B. Layer A derives from
56 20th century shepherd activities along with some redeposited Early Upper Palaeolithic (EUP)
57 artefacts. The underlying Layer B contains a rich EUP archaeological record with abundant
58 zooarchaeological remains, charred seeds and charred wood, lithic artefacts, and some isolated
59 hominin remains (Stutz et al., 2015). Macrobotanical analyses from flotation samples at MHM
60 are currently in preparation for publication. The site has been dated with radiocarbon assays
61 on ABOx-pretreated wood charcoal samples, indicating an occupation concentrated between
62 44.5-40.0 ky BP (Fig. 3, Table 1). MHM is notably the sole EUP cave site excavated in the Jordan
63 Valley, since Emireh Cave was investigated in the 1920's (Shea et al., 2019; Stutz et al., 2015;
64 Stutz and Nilsson Stutz, 2017).

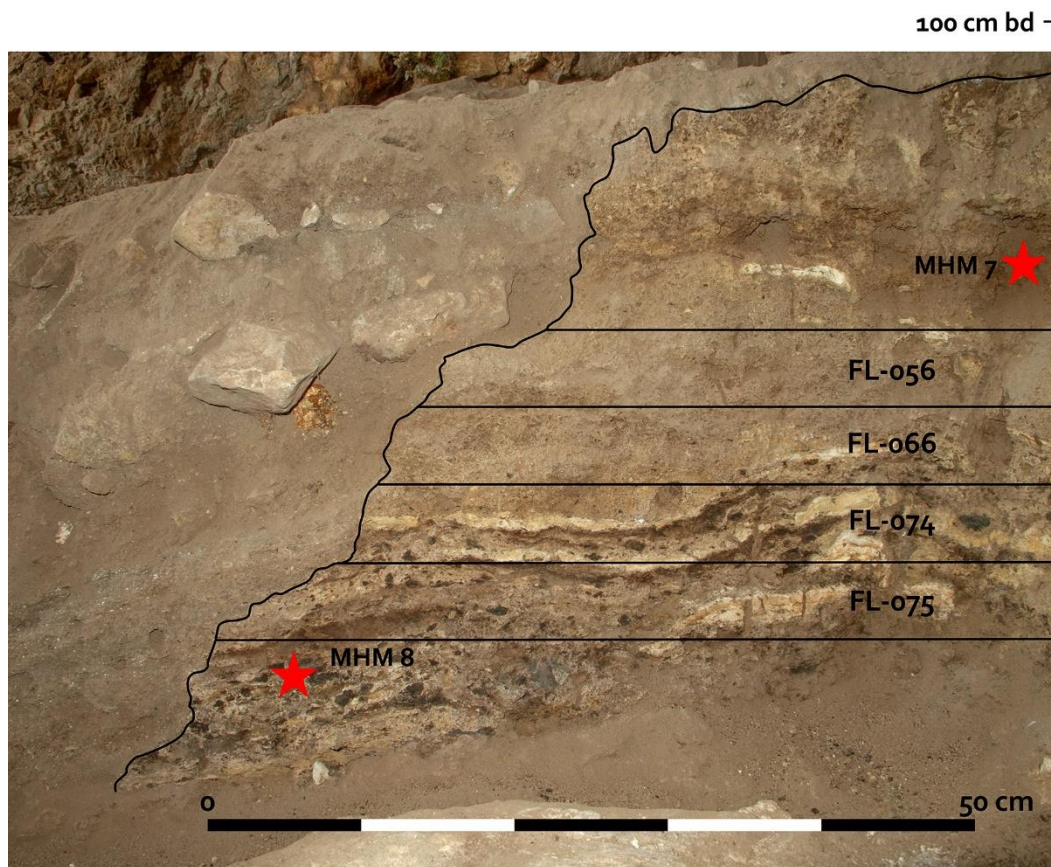


65

66 **Fig. 1.** Map of the Levant marked with important Late Middle Palaeolithic (LMP, ca. 70-48 ka) and earliest
67 Upper Palaeolithic (EUP, circa 47-40 ka) sites. MHM-Mughr el-Hamamah; 1 & 2-Tor Faraj (LMP) and Tor
68 Fawwaz (EUP); 3-Tor Sadaf (EUP); 4-Boker Tachtit (EUP); 5-Far'ah II (LMP); 6-Kebara Cave (LMP-EUP); 7 &

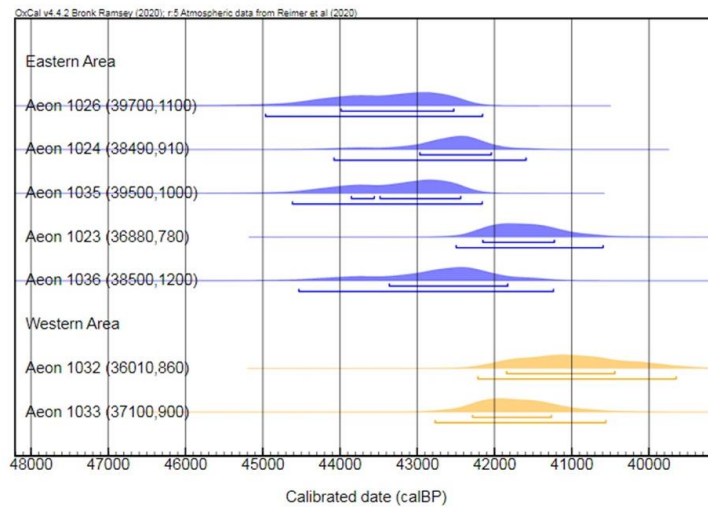
69 8 - Amud Cave (LMP) and Emireh Cave (LMP-EUP); 9-Manot Cave (EUP); 10-Ksar Akil Rockshelter (LMP-
70 EUP); 11-Üçağızlı Cave (EUP); 12-Umm el-Tlel (LMP-EUP). Basemap by user Fulvio314 on it.wikipedia.org,
71 available on Wikimedia. Commons under a CC.3.0. Unported. License

72 Despite the apparent good preservation of the archaeological assemblage in Layer B, field
73 observations noted some modern-era disturbances related to the later occupation of the cave
74 by shepherds during the 20th century (Fig. 2). Modern alterations of cave deposits caused by
75 shepherds are common, and they have been reported in several studies (i.e., Kehl et al, 2016;
76 Kadowaki et al. 2021). This disturbance also called into question the reliability of the presence
77 of plant microremains (phytoliths) in the EUP levels and their possible origin from the
78 shepherd's activities. Other observations were made relating to the uneven preservation of the
79 organic remains. For example, bone appeared to be better preserved in the eastern area while
80 charred plant remains were better preserved in the western area of the cave. Hence, to
81 correctly understand the activities and use of plants in the cave by EUP occupants, it
82 is essential to clarify the post-depositional processes affecting the archaeological deposits and
83 assess the degree to which shepherds disturbed the archaeological record of Layer B.



84

85 **Fig. 2.** Western section of square B2. Irregular solid line shows the cut into Early Upper Palaeolithic Layer
86 B, with the overlying recent Layer A. The stars mark the west-east and vertical coordinates of carbonized
87 wood radiocarbon samples MHM7 and 8. The flotation (FL) samples mark the arbitrary 5 cm levels of in
88 situ layer B material sampled in the adjacent (within-the-section) subsquare B1b, which yielded some of
89 the carbonized wild legume seeds and pistachio shell fragments described in the text. Micromorphology
90 sample 3 is from square B2a, directly in front of the section through the bedded hearth features visible
91 in the photograph. This sample captures bedded combustion material interstratified with a silt
92 component (see text). As in typical complicated, diagenetically altered Pleistocene cave deposits, it was
93 not possible to follow individual combustion features laterally. Thus, carbonized botanical material the
94 stratified combustion features were sampled in FL-066, 074 and 075, in order to obtain a macrobotanical
95 sequence over a relatively well-preserved portion of the Layer B deposits.



97

98 **Fig. 3.** Probability distribution function of the calibrated dates from Table 1 in blue dates related to
 99 samples from the Eastern Area and in orange the samples from the Western Area.

100

	MHM #	Sub-square	East coord.	South coord.	Depth (BD)	Comment	Lab Number	ABOx Comb. T °C	¹⁴ C Age ± 1σ year BP	C %	Calibrated range ±1σ year BP	Calibrated range ±2σ year BP
Eastern area main deposits	MHM 5-325	B5c	5	61	112	under limestone	Aeon 1026	625	39700 ± 1100	38.6	43000 - 42500	45000 - 42150
	MHM 4	C5a	22	18	124	under Hearth 1	Aeon 1024	325	38490 ± 910	54.3	43000 - 42000	44100 - 41550
	MHM 10-325	B5d	55	85	129	under limestone with bone and flint	Aeon 1035	325	39500 ± 1000	55.3	43900 (11.9%) 43550 43500 (56.4%) 42400	44650 - 42150
	MHM 2	C5a	23	40	131.5	under Hearth 2	Aeon 1023	325	36880 ± 780	53.8	42150 - 41200	42500 - 40550
	MHM 11	C5a	6	34	134.5		Aeon 1036	325	38500 ± 1200	55.1	43400 - 41800	44550 - 41200
Western area	MHM 7	B2a	0	0	117	in phosphatised upper layer B	Aeon 1032	325	36010 ± 860	50.9	41850 - 40400	42250 - 39600
	MHM 8	B2d	90	57	141	from hearth layers under rock	Aeon 1033	325	37100 ± 900	52.9	42300 - 41250	42800 - 40550

101 **Table 1.** Radiocarbon dates of MHM site. Non identified wood charcoal samples were processed applying
 102 ABOx procedure. Temperature for combustion is given in the table (ABOx Comb. T °C). Calibrated ranges
 103 are rounded to nearest 50y. Calibrated ages were obtained using the calibration program OxCal v4.4.5
 104 Bronk Ramsey (2020) and with the atmospheric calibration curve of Reimer et al. (2020).

105 Bearing in mind the complexity and different origins (natural and anthropogenic) of the post-
 106 depositional processes, it is key to apply a multi-proxy approach to reconstruct the biography
 107 of the deposit, as well as the state of preservation of the different archaeological traces.
 108 Microarchaeology provides the tools to achieve this purpose, as it studies the invisible record
 109 that makes up the macroarchaeological record and the sedimentary matrix in which it is
 110 buried. Microarchaeology groups several high-resolution techniques, such as
 111 micromorphology, which sometimes requires specific extraction methods (Weiner, 2010). The
 112 combination of different high-resolution techniques provides important information from many

113 different perspectives. This allows us to reconstruct the processes that led to the formation of
114 the archaeological deposit and the plant-related activities that took place at the site.

115 To understand the post-depositional processes at MHM Layer B and the state of preservation of
116 the archaeological record (macro and micro), we used a microarchaeological multi-proxy
117 approach, which included micromorphology, Fourier Transformed Infrared Spectroscopy (FTIR),
118 phytoliths and faecal spherulites analyses.

119 **2. Materials and Methods**

120 *2.1 Micromorphology*

121 Blocks of intact sediments (n=14) (Fig. 4) were collected for micromorphological analysis with
122 the aim of understanding the formation and post-depositional processes of specific contexts
123 (e.g., combustion features). The blocks were jacketed in plaster for transport to the Boston
124 University Microstratigraphy Laboratory where they were embedded in a mixture of polyester
125 resin and acetone (ratio 70:30). Hardened blocks were sliced with a rock saw to obtain 8x6 cm
126 chips, which were processed into thin section (30 μm thickness). Thin sections (n=21) were
127 analysed using a petrographic microscope (magnifications 25x, 50x, 100x, 200x, 400x).
128 Micromorphological descriptions are based on established literature (Macphail and Goldberg,
129 2017; Nicosia and Stoops, 2017; Stoops, 2021; Stoops et al., 2018). Considering that similar
130 depositional units occur repeatedly throughout the sampled contexts, we grouped
131 micromorphology samples under different microfacies types (MFT), according to the
132 description given by Flügel (2004: 1): “the total of all sedimentological and paleontological data
133 which can be described and classified from thin sections, peels, polished slabs or rock
134 samples”. This choice was dictated by the aim of understanding the post-depositional
135 processes in terms of lithological units (e.g., Layer A and Layer B at the macroscopic scale of
136 observation) and location within the cave (east vs. west), rather than systematically sample and
137 describe all micro-contexts from an anthropogenic perspective. In doing so, we followed
138 previous micromorphological studies of cave sites (Goldberg et al., 2009, 2015).

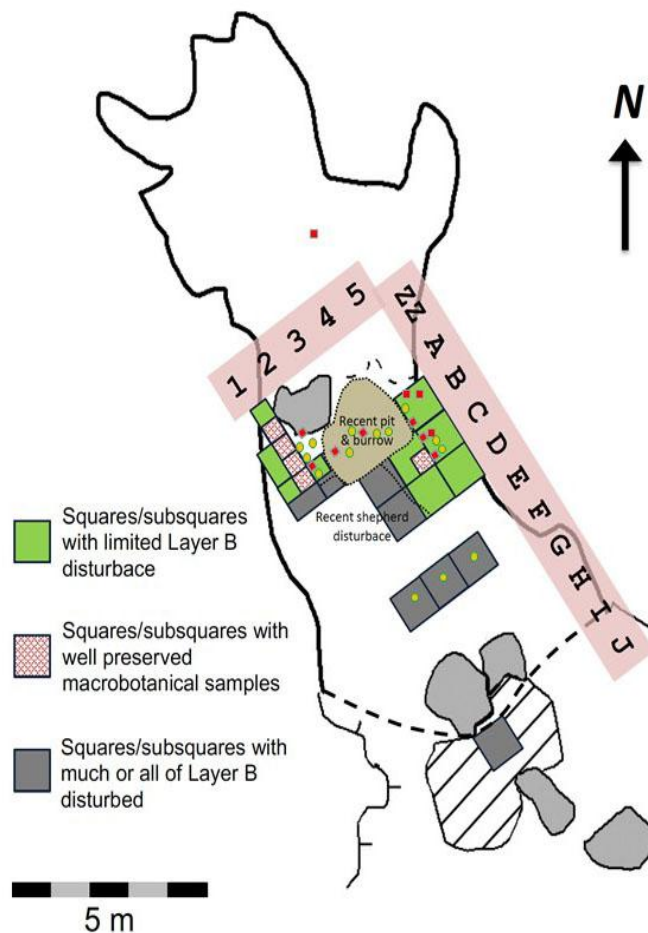
139 *2.2 FTIR*

140 68 bulk sediment samples were analysed using FTIR, which provides a quantitative assessment
141 of the gross mineral composition of sediments. FTIR helps us to better understand the
142 diagenetic processes that may have altered some of the archaeological remains. Seven samples
143 were collected from Layer A, 58 from Layer B, 1 from the surface (sample C9), and two that
144 could not be securely related to Layers A or B (samples F5 and F2) (Fig. 4). Samples were
145 collected from grid squares A1, A2, B2 and B3 located on the western area inside the cave;
146 squares B4, B5, and C5 in the eastern area inside the cave, and finally from squares F2, F3 and
147 F4, representing a 1x3m sounding just inside the dripline of the cave (Fig. 4). Additionally,
148 samples from squares A1 and A2 were prioritised due to the good associated preservation of
149 charred plant remains (seeds).

150 The methods used follow those of Weiner (2010). Tens of micrograms of archaeological
151 sediment were homogenised with KBr to obtain the pellets. Infrared spectra were obtained in
152 transmission mode using a Nicolet iS5 spectrometer at 4 cm^{-1} resolution and in 32 scans in the
153 4000-400 cm^{-1} spectral range. To assess the origin of calcite, when present, we applied the
154 infrared grinding curve method developed by Regev et al. (2010) based on the measurement of
155 the ν_2 and ν_4 intensity (874 and 713 cm^{-1} , respectively) normalised to the ν_3 intensity (1420 cm^{-1}).
156 Normalised intensity values were compared with reference grinding curves published in
157 Regev et al. (2010). Band shifts of clay minerals exposed to elevated temperatures, described
158 by Berna et al. (2007), were used to determine the possible thermal alteration of clay minerals
159 in the sediments. Additionally, the FTIR reference collection of standard materials provided by

160 the Kimmel Center of Archaeological Science, Weizmann Institute of Science was consulted
161 (<http://www.weizmann.ac.il/kimmel-arch/infrared-spectra-library>).

162



163

164 **Fig. 4.** Map of the cave with the provenience of block samples (red squares) for micromorphological
165 analyses, and loose samples (yellow dots) for microarchaeological analyses. Detailed information
166 regarding samples provenience (square, subsquare and layer) is given in Table 2 and 3.

167 2.3 Phytoliths and faecal spherulites

168 The 68 sediment samples analysed by FTIR were also analysed for phytoliths and faecal
169 spherulites.

170 Phytolith extraction was carried out following the methodology of Katz et al. (2010). Between
171 20 and 50 mg of sediment were placed in a 0.5 ml Eppendorf tube and 50 μ l of HCl 6N were
172 added. After the reaction disappeared, 450 μ l of sodium polytungstate solution (SPT)
173 $[\text{Na}_6(\text{H}_2\text{W}_{12}\text{O}_{40})\cdot\text{H}_2\text{O}]$ with a density of 2.4 g/ml were added. The tube was vortexed and
174 sonicated for 10 minutes and then centrifuged for five minutes at 5000 rpm. The supernatant
175 was removed and transferred to another tube. 50 μ l of the aliquot were placed on a
176 microscope slide and covered with a 24x24 mm coverslip. Phytoliths present in 20 visual fields
177 at 200x were counted for phytolith quantification. Morphological identification was based on
178 our own modern reference collection (www.phytcore.org) as well as standard literature
179 (Mulholland and Rapp, 1992; Piperno, 2006; Twiss, 1992). The nomenclature of the phytoliths
180 followed, whenever possible, the International Code for Phytolith Nomenclature (ICPN 2.0,
181 Neumann et al., 2019). Generally, a minimum number of 200 recognisable phytoliths is

182 desirable to obtain a reliable phytolith morphological interpretation (Albert and Weiner, 2001).
 183 In those cases where the minimum number of 200 phytoliths was not reached, we included
 184 samples with >80 recognisable morphotypes. This follows the results obtained by Rodríguez-
 185 Cintas et al. (2020), where it was shown that samples with lower amounts of phytoliths
 186 (between 50-200) had similar distribution of the dominant morphotypes to samples with
 187 higher numbers from the same sampled context.

188 High concentrations of faecal spherulites are associated with the dung of certain ruminants
 189 (Shahack-Gross et al., 2011), and their occurrence in sediments is an excellent biomarker for
 190 the presence of livestock. For this reason, they were used to delimit the recent disturbance
 191 caused by the herders. The methods used follow Gur-Arieh et al. (2013). Between 30 and 40
 192 mg of dried sediment is sieved through a 150 µm sieve, to remove particles >150 µm. After
 193 that, 500 µl of SPT with a density of 2.4 g/ml was added and the sample was sonicated for 10
 194 minutes to disaggregate all the elements. 50 µl of the solution was placed on a microscope
 195 slide and covered with a 24x24 mm cover-slide. Microremains were identified under polarised
 196 light at 400x. Along with faecal spherulites, we also looked for ash pseudomorphs (major
 197 component of wood ash).

198 3. Results

199 3.1 Micromorphology

200 Micromorphology samples were grouped under four microfacies types (MFT) (Table 2): silty
 201 clay, silt, dispersed anthropogenic components, and bedded anthropogenic components. The
 202 latter two include a subtype characterised by extensive diagenesis, represented by total
 203 absence of bone. Descriptions and terminology follow Stoops (2021).

204

205

MFT name	Description	Process	Sample # (square/layer)
Silty clay	<p>c/f related distribution: single-spaced to open porphyric (within aggregates).</p> <p>Structure and voids: crumb microstructure with compounds and complex packing voids; channel microstructure with channels.</p> <p>Coarse fraction: silt-sized, sub-angular quartz grains (dominant); medium sand-sized sub-rounded quartz grains (few); charcoal fragments (few); bone fragments (very few).</p> <p>Fine fraction: brown to reddish clay with speckled and grano-striated b-fabric.</p> <p>Pedofeatures: phosphate intergrowths; Fe-Mn nodules; silt infillings.</p>	Colluvium, bioturbation, dissolution	9 (A2/Layer B)
Silt	<p>c/f related distribution: monic (silt beds); double-spaced coarse enaulic (phosphate beds).</p> <p>Structure and voids: single-grain microstructure with simple packing voids (silt</p>	Sheetwash, dissolution	3 (B2/Layer B)

	<p>beds); intergrain microaggregate microstructure with complex packing voids (phosphate beds).</p> <p>Coarse fraction: fine silt-sized sub-angular quartz grains (very dominant).</p> <p>Fine fraction: phosphate crystals, no b-fabric.</p> <p>Pedofeatures: phosphate nodules.</p>		
Dispersed anthropogenic components	<p>c/f related distribution: single-spaced to open porphyric (within aggregates).</p> <p>Structure and voids: crumb microstructure with compound and complex packing voids; channel microstructure with channels.</p> <p>Coarse fraction: silt-sized, sub-angular quartz grains (dominant); medium sand-sized sub-rounded quartz grains (few); limestone pebbles (few); flint flakes (very few); bone fragments (frequent); charcoal fragments (few).</p> <p>Fine fraction: pale-brown to brown clay with faint or speckled b-fabric; dung spherulites.</p> <p>Pedofeatures: phosphate impregnations, intergrowths and nodules; calcium carbonate intergrowths and infillings; microfauna channels and burrows.</p>	Combustion, bioturbation, dissolution	1 (B5), 2 (B5), 12 (C5) (all Layer B)
Dispersed anthropogenic components (no bone)	<p>c/f related distribution: single-spaced to open porphyric (within aggregates).</p> <p>Structure and voids: crumb microstructure with compound and complex packing voids; channel microstructure with channels.</p> <p>Coarse fraction: silt-sized, sub-angular quartz grains (dominant); medium sand-sized sub-rounded quartz grains (few); limestone pebbles (few); flint flakes (very few); charcoal fragments (few); shell fragments (very few, samples 4 and 5).</p> <p>Fine fraction: pale-brown to brown clay with faint or speckled b-fabric; dung spherulites, crystallitic b-fabric (samples 4 and 5).</p> <p>Pedofeatures: extensive phosphate impregnations, intergrowths and nodules; microfauna channels and burrows.</p>	Combustion, bioturbation, dissolution	3 (B2/Layer B), 4 (B2/Layer A), 5 (B2/Layer A), 14 (B3/Layer A), 15 (B3/Layer A) (note that samples 14 and 15 appeared in the field to consist of redeposited cemented blocks originating from Layer B)
Bedded anthropogenic components	<p>c/f related distribution: single-spaced to open porphyric (within aggregates).</p>	Combustion, dissolution	8 (B5), 11 (C5), 16 (C5) (all Layer B)

	<p>Structure and voids: crumb microstructure with compound and complex packing voids; channel microstructure with channels and chambers.</p> <p>Coarse fraction: silt-sized, sub-angular quartz grains (dominant); medium sand-sized sub-rounded quartz grains (few); limestone pebbles (few); flint flakes (very few); bone fragments (frequent); charcoal fragments (few); phytoliths (very few).</p> <p>Fine fraction: pale-brown to reddish clay with faint or speckled b-fabric.</p> <p>Pedofeatures: phosphate intergrowths and nodules.</p>		
Bedded anthropogenic components (no bone)	<p>c/f related distribution: single-spaced to open porphyric (within aggregates).</p> <p>Structure and voids: crumb microstructure with compound and complex packing voids; channel microstructure with channels and chambers.</p> <p>Coarse fraction: silt-sized, sub-angular quartz grains (dominant); medium sand-sized sub-rounded quartz grains (few); limestone pebbles (few); flint flakes (very few); charcoal fragments (few); phytoliths (very few).</p> <p>Fine fraction: pale-brown to reddish clay with faint or speckled b-fabric.</p> <p>Pedofeatures: extensive phosphate intergrowths and nodules.</p>	Combustion, dissolution	6 (A2), 7 (A2) (Layer B)

206 **Table 2.** Micromorphological descriptions of the MFTs. The terminology follows Stoops (2021).

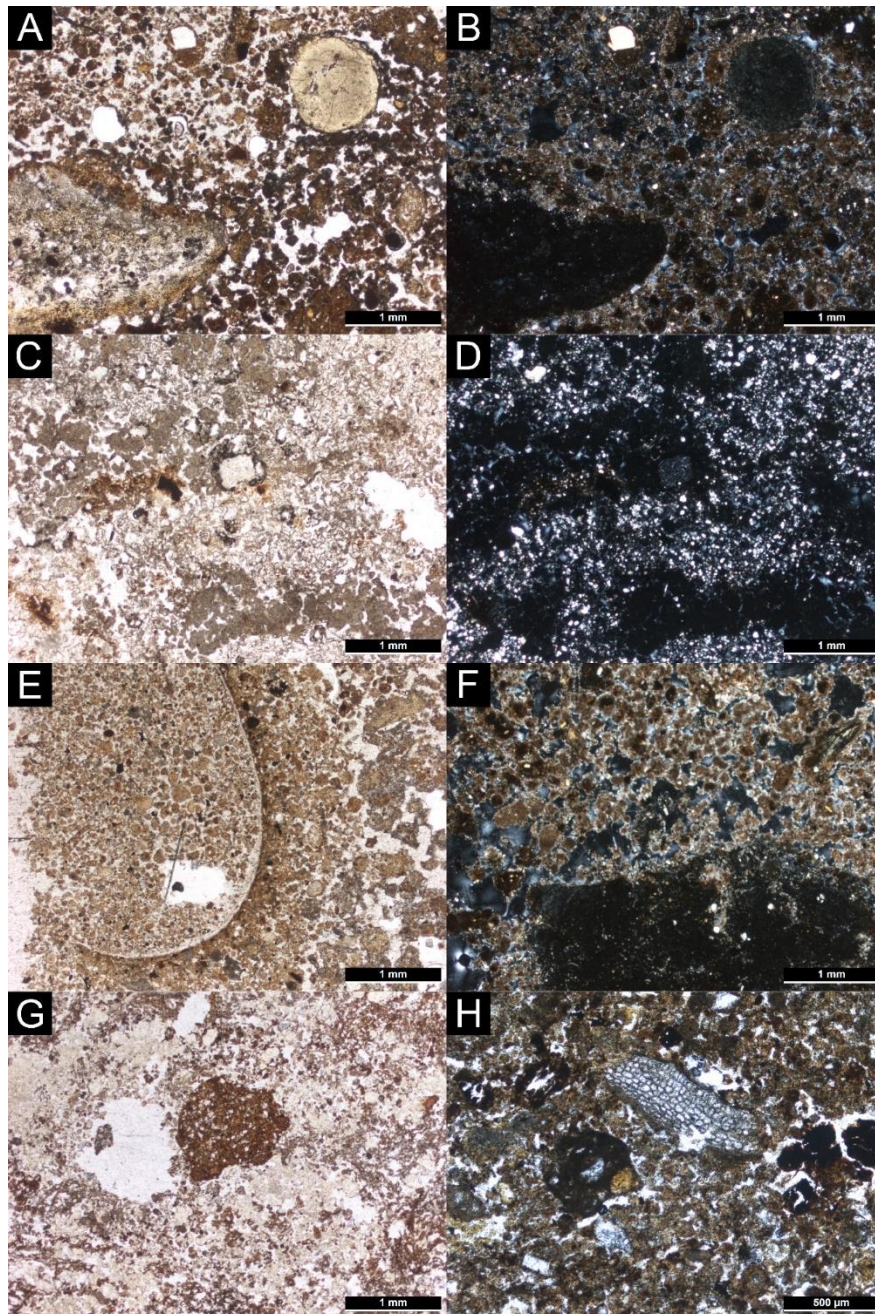
207 **3.1.1 Silty clay**

208 Sample 9 from square A2 (western area) (Fig. 4) is composed mainly of small aggregates of silty
209 clay, characterised by overall high porosity although in places they show evidence of
210 compaction (without bedding). Clay minerals are brown to reddish in colour and exhibit
211 speckled birefringence fabric (b-fabric), and grano-striated b-fabric around quartz grains.
212 Anthropogenic materials include charcoal fragments, which occur in small numbers throughout
213 the sample, and very few fragments of bone. Calcium carbonate is absent, whereas
214 pedofeatures include phosphate nodules and iron-manganese nodules (Fig. 5a and 5b). Rare
215 silt infillings are also present.

216 **3.1.2 Silt**

217 In square B2 (western area) (Fig. 4), part of sample 3 exhibits alternating beds of pure quartz
218 silt and phosphate nodules (Fig. 5c and 5d). The latter are grey in plane polarised light and
219 isotropic in cross polarised light and appear substantially different from calcium phosphate

220 nodules observed ubiquitously in all other contexts. No anthropogenic components were
221 observed.



222

223 **Fig. 5.** Photomicrographs of micromorphology thin sections. A-B: authigenic phosphate nodules; note
224 their isotropic nature in cross-polarised light (B); C-D: alternating beds of authigenic phosphate nodules
225 and silt, the latter exhibits bright interference colour in cross-polarised light (D); E: burrow filled with clay
226 aggregates; F: aggregates of recrystallised ash in cross-polarised light; G: rounded pellet of red silty clay
227 embedded in a matrix rich in secondary phosphates; H: ashed plant fibre (now phosphatised calcium
228 carbonate) retaining the original cellular structure.

229 *3.1.3 Dispersed anthropogenic components*

230 Most contexts are grouped under this MFT. Aggregates of silty clay, including large fragments of
231 bone (some of which are burnt) and charcoal, are characterised by high porosity and little
232 compaction and are dispersed throughout the sample, with clear evidence of bioturbation (Fig.

233 5e). Burrows and channels produced by microfauna are common in all samples and in places
234 contain calcitic dung spherulites, including in the groundmass in samples 4 and 5 (square B2)
235 (Fig. 4). Furthermore, samples 4 and 5 are rich in shells of land snails, which appear to be well
236 preserved based on their interference colour. Aggregates of recrystallised and phosphatised
237 calcium carbonate ash and/or secondary calcium carbonate infillings are common in a few
238 samples (Fig. 5f). Large (cm-sized) aggregates and smaller rounded pellets of reddened silty
239 clay are common in all samples, and exhibit different types of b-fabric, from faint to speckled
240 (Fig. 5g). Very few flint artefacts occur as well. More than half of the samples are assigned to a
241 subtype of the MFT where no bone or calcium carbonate is preserved (except for land snail
242 shells in samples 4 and 5) and phosphate intergrowths and nodules occur throughout the thin
243 section.

244 3.1.4 Bedded anthropogenic components.

245 Five samples exhibit beds of phosphatised ash and/or red clay. There is a marked distinction
246 between contexts where bone is not preserved (MFT subtype characterised by extensive
247 diagenesis), rich in authigenic phosphate nodules and intergrowths of different mineralogy, and
248 contexts where bone is well preserved, together with phosphatised calcium carbonate ash,
249 limestone pebbles with reaction rims, and secondary calcium carbonate. Two samples exhibit
250 ashed and phosphatised calcium carbonate plant fibres (phosphatised calcium carbonate) that
251 retain the original cellular structure (Fig. 4H). Phytoliths occur in one context but are not clearly
252 visible due to stacking with phosphates. Red clay pellets are common, and in sample 16 red
253 clayey sediment occupies the entire lower portion of the thin section (Fig. 5). Post-depositional
254 processes include the dissolution of bone minerals and extensive precipitation of authigenic
255 phosphates, and bioturbation from microfauna.



256

257 **Fig. 6.** Scan of a representative thin section of the MFT characterised by bedded anthropogenic
258 components (sample MHM10 16a, square C5), showing loose charcoal, bone fragments, and red clay
259 pellets resting on top of a compact, reddened substrate (dashed line).

260 3.2 FTIR

261 Three mineralogical groups were identified through FTIR-analysis: silicates, carbonates, and
262 phosphates (Fig. 7).

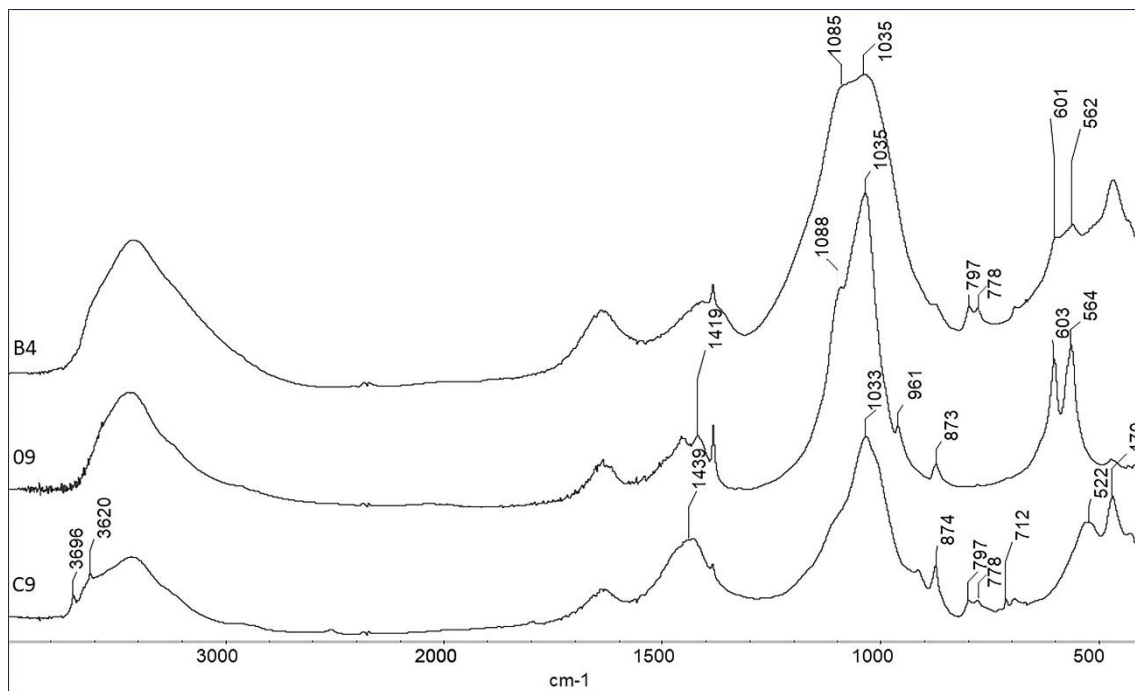
263 3.2.1 Silicates

264 Terra rossa clay is the largest silicate component and forms the sediment matrix (Table 3). Terra
 265 rossa is a silty to clayey reddish soil, composed of clay, quartz, calcite, and oxides, and is
 266 widespread through the Mediterranean area (Durn et al., 2014). Clay minerals identified in
 267 Layer B (squares A1 and A2) have a diagenetically altered structure (Table 3). Additionally, clay
 268 minerals showing thermal alteration are observed in samples from square C5 (eastern area),
 269 squares F2-4 (front sounding), square B2a (western area), and square B3 (central area) (Fig. 4,
 270 Table 3). Quartz is also present in all contexts (Fig. 7, Table 3).

271 Siliceous aggregates are present in almost all samples (Table 3). They are an important
 272 component of wood ash and consist of fine-grained crystalline minerals embedded into a
 273 biogenic silica matrix.

274 3.2.2 Carbonates

275 Calcite was documented in eight samples, mainly in squares F2, F3, and F4 (front sounding
 276 Layers A and B), but also in square B2a (western area, Layer B), and C9 (eastern area) (Fig. 7,
 277 Table 3). In all cases, calcite derived from wood ash. Two samples are associated with the MFT
 278 'dispersed anthropogenic components' (sample B1 from mixed Layer B material redeposited in
 279 Layer A fill; and the superficial sample C9) (Fig. 7, Table 3).



280
 281 **Fig. 7.** FTIR from different samples from MHM showing their main components: C9) unburnt
 282 clay (3696, 3620, 1033, 522, 470 cm^{-1}); geogenic calcite (1439, 874, 712 cm^{-1}); O9) carbonate
 283 hydroxylapatite (1419, 1035, 603, 564 cm^{-1}); B4) burnt clay (1035, 797, 778 cm^{-1}); apatite (601,
 284 562 cm^{-1}).

285

286 3.2.3 Phosphates

287 Authigenic phosphate minerals, such as carbonate hydroxylapatite, resulting from the
 288 interaction between phosphorous derived from the decay of organic material and calcite
 289 (Shahack-Gross et al., 2005), were identified in some samples where shepherds' disturbance
 290 was indicated by the identification of faecal spherulites. Yet, carbonate hydroxylapatite was
 291 detected in samples from the eastern area of the cave (square C5) and it is noteworthy that

292 these samples do not show spherulites. Additionally, sample 9, collected from the bedrock
 293 exposed in square A2, is composed of pure carbonated hydroxylapatite (Fig. 7, Table 3).
 294 Variscite and montgomeryite were observed in two samples from the western area (squares A1
 295 and A2) (Fig. 4, Table 3). These minerals result from the dissolution and recrystallisation of
 296 more soluble components (carbonates) as the pH of the sediments decreases (Weiner et al.,
 297 2002). Transforming apatite was noted in the eastern area of Layer B, squares B4 and B5 (Table
 298 3). Apatite is the most ubiquitous phosphate mineral in soils and can be composed of different
 299 mineral phases (apatite transforming) resulting from continuous dissolution and
 300 recrystallisation processes (Karkanis et al., 2002). Finally, amorphous calcium iron phosphate,
 301 probably an authigenic mineral that incorporates different elements, was detected in Layer B,
 302 squares A1, A2 and B1 (Table 3).

303 3.3 Faecal spherulites

304 Spherulites (Fig. 8 a) were documented in 20 samples (six from Layer A, 13 from Layer B, and
 305 in one that could not be assigned either to Layer A or B (F5 and F2) (Fig. 4, Table 3). Sample B9
 306 (square B4) is the only sample from Layer A where spherulites were not observed. In Layer B,
 307 they were observed in squares F3, F4, B2, A2 (western area), and B5 (Fig. 4, Table 3).
 308 Conversely, no ash pseudomorphs were observed in the samples.

Lab #	Square	Subsquare	Layer	Phytoliths per g. of sediment	#Phytolith identified	Spherulites per g. of sediment	Weathering (%)	FTIR
F1	F2	A-B	A	1,000,000	322	7,100,00	10.8	Cl(b), Ca(a), SA, Qz
F2	F3	C-D	B	408,000	184	887,000	4.2	Cl(b), Ca(a) CHA, Qz SA,
F3	F3	C-D	B	260,000	176	811,000	7.9	Cl(b), Ca(a), CHA, SA, Qz
F4	F4	C	A	770,000	262	1,000,000	5.1	Cl(b), Ca(a), SA, CHA, Qz
F5	F2	A-C	?	173,000	167	20,000	1.8	Cl(b), Ca(a), CHA, Qz SA
F6	F2	C-D	A	167,000	248	1,900,000	3.9	Cl(b), Si, Ca(a), Qz
F7	F2	C-D	?	95,000	241	0	5.9	Cl, Sanidine
F8	F4		B	104,000	204	959,000	4.7	Cl (b), SA, CHA, Qz
B1	B2	A	B	534,000	248	466,000	3.9	Cl (b), Ca(a), SA, CHA
B2	B2	A	B	13,500	22	0	18.5	Cl, SA, Qz
B3	B2	A	B	13,000	65	14,000	0.0	Cl, SA,
B4	B2	A	B	196,000	199	0	6.1	Cl(b), Ap(t) SA, Qz
B5	B2	A	B	123,000	229	0	24.2	Cl(b), Ap(t), SA, Qz, ACIP
B6	B3	B	B	113,000	65	44,000	3.0	Cl(b), SA, Qz, ACIP
B7	B3	B	A	377,000	224	830,000	4.7	Cl(b), SA, Qz, CHA
B8	B4	A	A	245,000	231	18,000	4.9	Cl, CHA, SA
B9	B4	A	A	95,000	205	0	3.3	Cl, SA, Qz, CHA

B10	B4	A	A	252,000	199	1,300,000	12.3	CI, CHA, SA
C1	C5	A	B	2,000	31	0	72.8	CI(b) SA, CHA
C2	C5		B	145,000	185	0	15.1	CI (b), SA, CHA
C3	C5	C	B	53,000	147	0	21.8	CI, SA, Qz, CHA?
C4	C5	A-C	B	22,000	85	0	19.1	CI, SA, Qz, CHA?
C5	C5	C	B	6,000	7	0	22.2	CI(b), SA, Lp
C6	C5	A	B	2,000	24	0	11.1	CI(b), CHA, SA
C7	C5	C	B	1,000	7	0	46.2	CI(b), CHA, SA?
C8	C5	A	B	3,000	9	0	35.7	CI, CHA, SA, Qz
C9	C5	surface	surface	86,000	81	0	2.4	CI, Ca, Qz,
1	A1	D	B	13,000	8	0	27.3	CI(t), Ap(t), ACIP
2	A1	D	B	0	0	0	0.0	CI(t), Qz, SA
3	A1	D	B	0	0	0	0.0	CI(t), Qz, CHA, SA
4	A1	D	B	0	0	0	0.0	CI(t), Qz, SA
5	A1	D	B	69,000	5	0	37.5	CI(t), Qz, SA
6	A1	D	B	0	0	0	0.0	CI(t), Qz
7	A1	D	B	0	0	0	0.0	CI(t), ACIP, Qz
8	A1	D	B	0	0	0	0.0	CI(t), ACIP, Qz
25B	A1	D	B	0	0	0	0.0	CI(t), Mo(t), SA
26	A1	D	B	0	0	0	0.0	CI(t), SA, ACIP
27	A1	D	B	0	0	0	0.0	CI(t), SA, ACIP
28	A1	D	B	0	0	0	0.0	CI(t), SA, ACIP
29	A1	D	B	15,000	100	0	20.3	CI(t), Qz
30	A1	D	B	0	0	0	0.0	Va, SA
31	A1	D	B	0	0	0	0.0	Va, SA
50	A1	B	B	0	0	0	0.0	CI(t), ACIP, SA
51	A1	B	B	36,000	102	0	13.9	CI(t), ACIP, SA
52	A1	B	B	0	0	0	10.8	CI(t), ACIP, SA
9	A2	C	B	0	0	0	0.0	CHA
10	A2	C	B	0	0	0	0.0	CI(t), ACIP, SA, Qz
11	A2	C	B	0	0	0	0.0	CI(t), CHA(t), ACIP
12	A2	C	B	0	0	0	0.0	CI(t), Qz, ACIP
13	A2	C	B	0	0	0	0.0	CI(t), Qz, ACIP, SA
14	A2	C	B	0	0	0	0.0	CI(t), Qz, ACIP
15	A2	C	B	24,000	4	0	0.0	CI(t), Qz, ACIP
16	A2	C	B	7,000	7	0	30.0	CI(t), Qz, ACIP

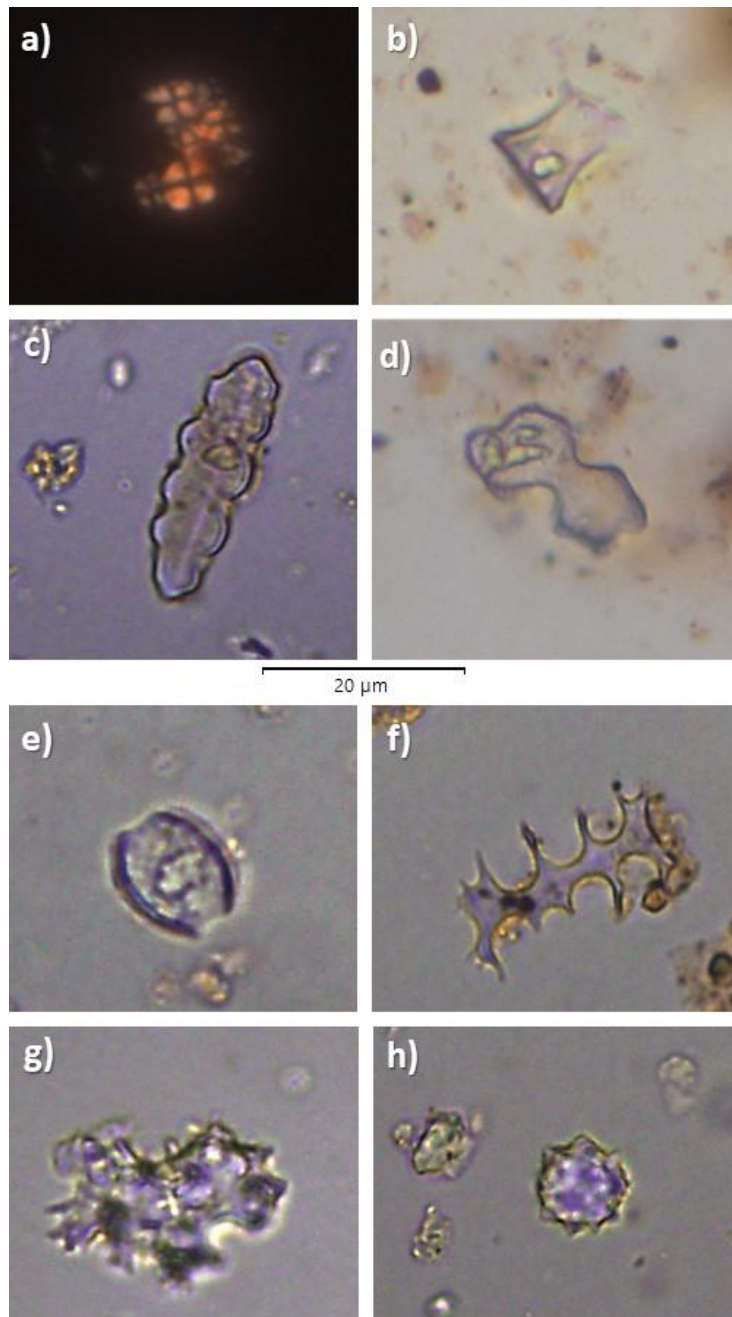
17	A2	C	B	0	0	0	0.0	Cl(t), Qz, ACIP, SA
18	A2	C	B	0	0	0	0.0	Cl(t), ACIP, Ap(t), SA
19	A2	C	B	212,000	192	374,000	0.0	Cl(t), SA, Qz, ACIP
20	A2	C	B	23,000	5	0	0.0	Cl(t), SA, ACIP, Mo
21	A2	C	B	0	0	0	0.0	Cl(t), Qz, SA, ACIP
22	A2	C	B	34,000	15	0	0.0	Cl(t), SA, ACIP, Mo(t)
38	B4	B	B	1,101,000	196	1,750,000	9.7	Cl, Ap(t), SA
40	B4	B	B	211,000	123	85,000	3.1	Ap(t), Cl(t), SA
32	B5	B	B	25,000	14	30,000	0.0	Cl, Ap(t), SA
33	B5	B	B	79,000	36	89,000	0.0	Cl, Ap(t), SA
34	B5	B	B	0	0	0	0.0	Cl, Ap(t), SA
35	B5	B	B	45,000	100	0	5.7	Cl, Ap(t), SA
36	B5	B	B	203,000	50	1,140,000	3.8	Cl, Ap(t), SA
37	B5	B	B	311,000	101	394,000	4.7	Cl(t), Ap(t), SA
39	B5	A	B	41,000	8	0	0.0	Cl, Ap(t), SA

309 **Table 3.** List of the 68 samples analysed and their provenience, as well as the results: estimated number
310 of phytoliths per gram of material, number of phytoliths morphologically identified, percentage of
311 weathered phytoliths (chemical alteration), estimated number of faecal spherulites per gram of material,
312 and FTIR results. Ca: Calcite; Cl: clay; SA: siliceous aggregates; CHA: carbonate hydroxylapatite; Si: silica;
313 Qz: quartz; ACIP: amorphous calcium iron phosphate; Ap: apatite; Mo: montgomeryite; Va: variscite; (a):
314 ash derived; (b) burnt; (t): transforming

315

316 3.4 Phytoliths

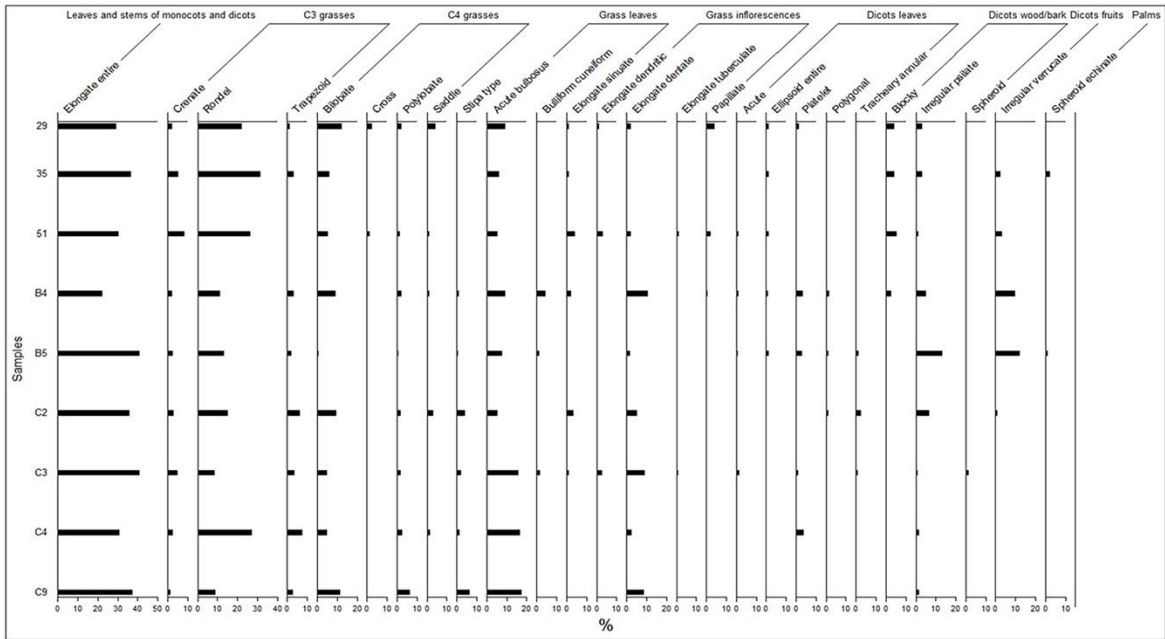
317 Phytoliths were identified in both Layers A and B. Samples from Layer A show concentrations of
318 phytoliths per gram of sediment between 86,000 (C9) and 1,000,000 (F1) (Table 3) and are
319 associated with the presence of spherulites, except for sample B9 from the eastern area
320 (square B4), which yielded a lower concentration of phytoliths and no spherulites (Table 3).
321 Phytolith concentrations in Layer B ranged from 7,000 (16, square A2) to 196,000 (B4, square
322 B2) (Table 3). The percentage of weathered phytoliths varies between 5.7% and 24.2% (Table
323 3). PCA analysis was performed in samples with >80 morphotypes identified, and the
324 distribution of morphotypes shows that samples from Layer A cluster together (with the
325 exception of sample F1), with a higher proportion of grasses, while samples from Layer B have
326 higher proportions of dicot morphotypes (Fig. 9).



327

328 **Fig. 8.** Microphotographs of faecal spherulites and phytoliths. Images taken at 400x: a) faecal spherulites
 329 from sample B7; b) GSSCP RONDEL pyramidal with a keeled top from sample 19; c) CRENATE from sample
 330 B4; d) GSSCP BILOBATE with the lobes ends convex, from sample 33; e) SADDLE from sample 29; f) ELONGATE
 331 DENDRITIC from sample C3; g) IRREGULAR VERRUCATE characteristic of dicots fruits from sample B4; h)
 332 SPHEROID ECHINATE characteristic palm phytolith from samples 51.

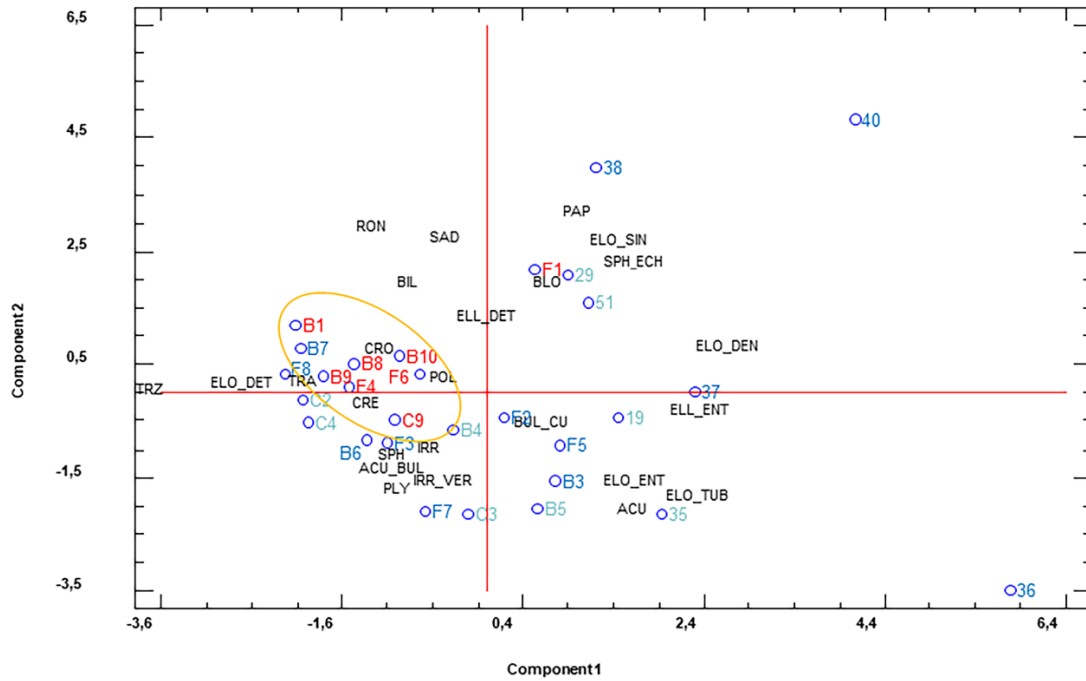
333 Layer A shows a high number of faecal spherulites and therefore these levels were interpreted
 334 as highly disturbed and were not included in our phytolith study of the EUP layers. On the
 335 contrary, most samples from layer B did not show the presence of spherulites and were
 336 interpreted as not having been disturbed by intrusive microbotanical traces. Therefore, our
 337 study focused on those Layer B-associated samples where faecal spherulites were absent. In
 338 these spherulite-free Layer B samples, 24 different morphotypes were identified (Table 4.
 339 Phytoliths morphologically identified in undisturbed samples from Layer B, botanical attribution, and
 340 average presence in the samples.



341

342 **Fig. 10.** Plot with then relative abundance of each morphotype identified in the undisturbed samples
 343 from Layer B, grouped accordingly to their attributions.

344). Whenever possible, morphotypes were grouped into different categories based on their
 345 taxonomic and anatomical provenance: Poaceae (C_3 and C_4), Poaceae leaves/stems, Poaceae
 346 inflorescence, dicots wood/bark, dicot leaves, dicot fruits, and palms. ELONGATE ENTIRE was not
 347 included in these groups because, although this morphotype is commonly produced in the
 348 stems of grasses and sedges, it can also be found in dicotyledonous plants in lesser numbers
 349 (ICPN 2.0, Neumann et al., 2019) (Fig. 11). The relative abundance of each morphotype
 350 identified can be found in the supplementary material.



351

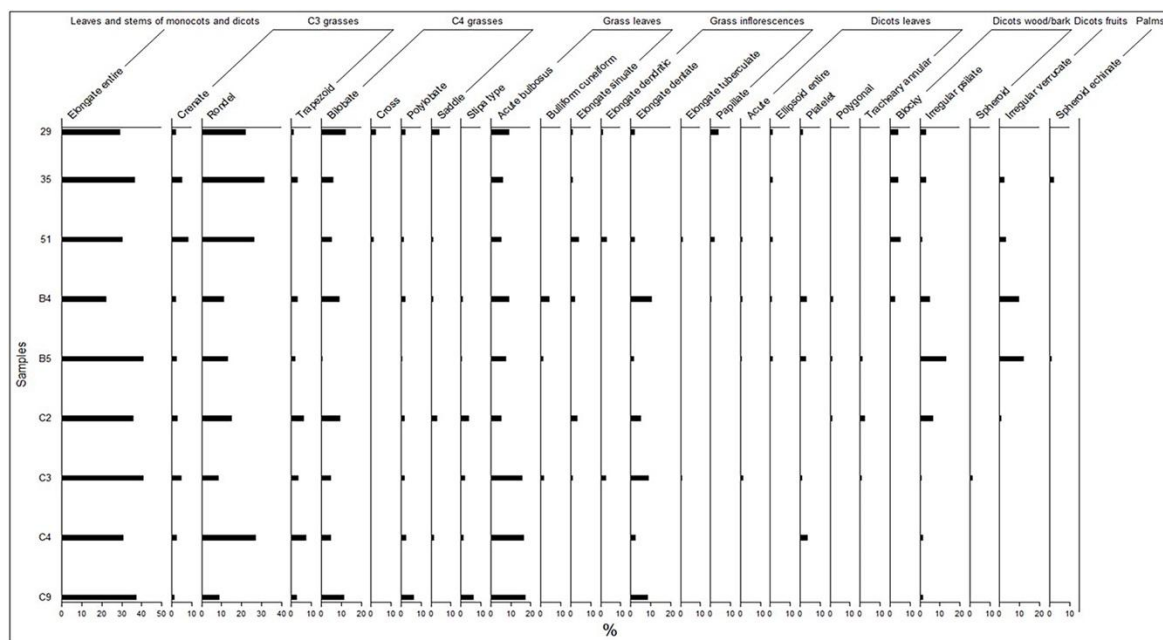
352 **Fig. 9.** PCA run over morphotypes and samples from Layers A and B (n=29). Sample provenance is
 353 indicated by colours: red: Layer A; blue: disturbed (presence of spherulites) Layer B; and green
 354 undisturbed (absence of spherulites) Layer B.

355

Morphotype	Botanical attribution	Average %
ELONGATE ENTIRE	Leaves and stems of monocots and dicots	33.6
RONDEL	C ₃ grasses	18.1
ACUTE BULBOSUS	Grass leaves	10.1
BILOBATE	C ₄ grasses	6.9
ELONGATE DENTATE	Grass inflorescences	5.1
IRREGULAR PSILATE	Dicots wood/bark	3.8
IRREGULAR VERRUCATE	Dicots Fruits	3.4
CRENATE	C ₃ grass leaves	3.3
BLOCKY	Dicots wood/bark	3.1
TRAPEZOID	C ₃ grasses	3.1
POLYLOBATE	C ₄ grasses	2.1
BILOBATE TRAPEZOID	Stipeae tribe	2.0
CROSS	C ₄ grasses	1.5
PLATELET	Dicots leaves	1.4
ELONGATE SINUATE	Grass leaves	1.3

SADDLE	C ₄ grasses	1.2
BULLIFORM CUNEIFORM	Grass leaves	0.9
ELLIPSOID ENTIRE	Dicots leaves	0.9
ELONGATE DENDRITIC	Grass inflorescences	0.8
PAPILLATE	Grass inflorescences	0.8
SPHEROID ECHINATE	Palms	0.7
ACUTE	Dicots leaves	0.5
TRACHEARY ANNULAR	Dicots leaves	0.5
POLYGONAL	Dicots leaves	0.5
SPHEROID	Dicots wood/bark	0.3
ELONGATE TUBERCULATE	Grass inflorescences	0.2

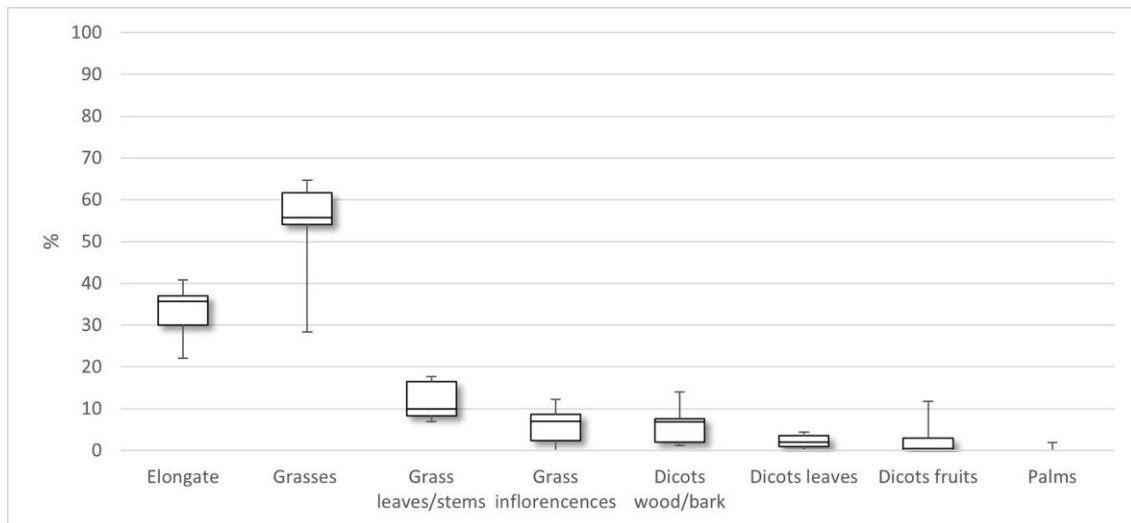
356 **Table 4.** Phytoliths morphologically identified in undisturbed samples from Layer B, botanical attribution,
357 and average presence in the samples.



358 **Fig. 10.** Plot with then relative abundance of each morphotype identified in the undisturbed samples
359 from Layer B, grouped accordingly to their attributions.
360

361 The most abundant morphotypes noted were the Grass Silica Short Cell Phytolith (GSSCP) from
362 the Poaceae family, particularly RONDEL (18.1%), and TRAPEZOID (3.1%) (Table 4, Fig. 8 b, c, Fig. 10
363 and Fig. 11). Also, CRENATE morphotype was documented (3.3%). These morphotypes are most
364 identified in C₃ grasses such as pooids, for example *Poa bulbosa* and *Dactylis glomerata*,
365 abundant in the area (Taifour and El-Oqlah, 2016). Other GSSCP identified were BILOBATE (6.9%)
366 (Fig. 8 d), POLYLOBATE (2.1%) and SADDLE (1.2%) (Table 4, Fig. 8 e and Fig. 10). BILOBATE are found
367 in the C₄ Panicoideae subfamily and in certain C₃ plants such as Stipeae tribe and
368 Arundinoideae subfamily (Chauhan et al., 2011; Shakoor et al., 2014). The BILOBATE identified,
369 with narrow lobes and trapezoidal section, has the typical characteristics produced by the
370 Stipeae tribe (Blinnikov, 2005; Fredlund and Tieszen, 1994) (Table 4, Fig. 10). Square C5

371 (eastern area) had a higher concentration of these morphotypes (>6%). SADDLES are widely
 372 produced by C₄ plants of the Chloridoideae and Bambusoideae subfamilies, and are associated
 373 with drier environments (Bremond et al., 2008; Fredlund and Tieszen, 1994). Phytoliths
 374 characteristic of the inflorescence of grasses were also identified (<12.2%) (Table 4, Fig. 11).
 375 This plant part is represented by ELONGATE with decorate margins: E. DENTATE (5.1%), E. DENDRITIC
 376 (0.8%) (Fig. 8 f) and E. TUBERCULATE (0.2%) and by PAPILLATE (Table 4).



377

378 **Fig. 11.** BoxPlot showing the percentage presence of the different phytoliths identified in undisturbed
 379 Layer B samples (n=9), grouped by their taxonomic and anatomical provenience in plants. Elongates have
 380 been kept separated as per their low taxonomic value. The mean values (mid-line), standard error ±
 381 (box) and standard deviation (whiskers) are given for the plant types and plant part.

382 Dicot phytoliths were present in samples from the western area, including sample 29 (square
 383 A1), samples B4 and B5 (square B2) and from the eastern area, sample 35 (square B5) with
 384 percentages ranging from 9% to 18% (Fig. 10). Within the dicots, morphotypes from wood and
 385 bark were more abundant (IRREGULAR PSILATE (3.8%) and BLOCKY (3.1%)) than those from leaves
 386 (PLATELET (1.4%), ELLIPSOID (0.9%), TRACHEARY ANNULAR (0.5%), POLYGONAL (0.5%) and SPHEROID
 387 (0.3%)). IRREGULAR VERRUCATE (Fig. 8 g), common in dicot fruits (Runge 1999), occurred mainly in
 388 samples B4 and B5 from square B2 (11.8%) (Fig. 10 and Fig. 11). Finally, SPHEROID ECHINATE (Fig. 8
 389 h), which is widely produced in palms (Albert et al., 2009) are also present in samples 51
 390 (square A1) and B5 (square B2), although at a low percentage (<2%) (Fig. 10 and Fig. 11).

391 4. Discussion

392 4.1 Sedimentary context

393 The mineralogical composition of the samples analysed in this study reflects the terra rossa
 394 sedimentary context of the site. This is supported by the occurrence of clay minerals in the FTIR
 395 spectra. The identification of authigenic phosphates, confirms the presence of components
 396 originated from the degradation of organic matter. Additionally, wood ashes are also part of
 397 the sediments as revealed by the presence of siliceous aggregates and pyrogenic calcite in the
 398 FTIR.

399 The crumb microstructure exhibiting different degrees of compaction and the grano-striated b-
 400 fabric of the silty clay sediment (sample 9, Layer B) can be associated to a certain degree of
 401 colluvial transport, possibly involving human agency in the case of dispersed anthropogenic
 402 components including charcoal, burnt bone, and red silty clay pellets (Layer B samples 1-3 and
 403 12 and Layer A/redeposited Layer B samples 4-5 and 14-15) (Goldberg et al., 2009). The
 404 bedded anthropogenic material, on the contrary, is the result of primary deposition by the EUP

405 occupants (Layer B samples 6-8, 11, 16). In the case of the silt MFT (observed in Layer B sample
406 3, square B2), the absence of fine fraction in the silt beds indicates that they were deposited by
407 low-energy water, as in sheetwash (Toffolo et al., 2017). Given that this sedimentary structure
408 occurs in only one in situ sample from Layer B, it is not possible to verify whether the
409 depositional process is localised, or it affected the entire cave.

410 4.2 Preservation

411 The results confirm the uneven preservation of the MHM EUP-associated Layer B deposit. Two
412 distinct areas can be identified.

413 4.2.1 Western area

414 Archaeological observations in the field noted the absence of bone, combined with
415 macroscopic white and yellow nodules suspected to be phosphate concretions. This suggested
416 post-depositional bone dissolution within square B2 (Stutz et al., 2015). The dissolution can be
417 explained by the presence of the low-energy water sources identified by micromorphology in
418 sample 3. In squares A1 and A2 both micromorphological and FTIR results highlight the
419 presence of phosphate minerals formed in low pH sediments, where bones tend to dissolve
420 (pH <7.2) (Weiner et al., 1993). This also explains the absence of calcium carbonate, the main
421 component of ash and the mineral from which these more insoluble minerals recrystallise
422 (Karkanas et al., 2002). Regarding the silty clay MFT (square A2), the rare silt infillings observed
423 reflect coarse water movement down the profile, whereas the iron-manganese nodules are
424 caused by the oxidation of ions mobilised by the decay of organic material (Vepraskas et al.,
425 2018).

426 More generally, cycles of wetting and drying favoured the nucleation of phosphate nodules,
427 which is related to the evaporation of water saturated in phosphate ions originating from the
428 dissolution of organic matter and/or bones (Karkanas et al., 2000; Shahack-Gross et al., 2004).
429 The intensity of post-depositional processes varies considerably within the western area. It
430 includes extreme results where no bone is preserved, and only extensive authigenic phosphate
431 intergrowths and nodules of variable mineralogy remain. The better-preserved samples show
432 aggregates of recrystallised calcium and phosphatised carbonate ash, as well as recent land
433 snail shells made of calcium carbonate. This high variability in the effects of diagenetic
434 alteration of the sediments is common in limestone and dolomite caves in the southern Levant,
435 as shown at sites such as Kebara, Hayonim, and Manot, located west of the Jordan Valley
436 (Albert et al., 2012; Berna et al., 2021; Mercier et al., 1995; Schiegl et al., 1996; Weiner et al.,
437 2007; Weiner et al., 1993; Weiner et al., 2002). Conversely, abundant, and well-preserved
438 wood charcoal (i.e., *Quercus* deciduous type, *Pistacia*, *Amygdalus*), charred seeds (i.e., large-
439 seeded legumes, *Pistacia*, *Ficus*) (White et al., 2019) and fruit and dicotyledonous phytoliths
440 are well represented in the western area. Therefore, our results suggest that post-depositional
441 processes in the western area would have affected the preservation of bones, but not the
442 macro- and microbotanical remains.

443 4.2.2 Eastern area

444 Interestingly, all the micromorphological samples from the eastern side of the cave (row 5 of
445 the site grid, Fig. 4) are clearly associated stratigraphically with Layer B, and they show bone
446 and (to a smaller extent) calcium carbonate preservation, whereas Layer B samples from the
447 western side are affected by bone dissolution and extensive phosphate growth. The Layer B
448 samples from square C5 show the presence of combustion features, mineralogically composed
449 of phosphates, particularly carbonate hydroxylapatite. Despite the presence of phosphates,
450 bones are well preserved in this area, which is consistent with Weiner et al. (1993), who show
451 that bones can be preserved in carbonated apatite contexts. Preliminary archaeobotanical

452 results from this area suggest that legume seeds and nutshells may be less abundant than in
453 the western area. Dicots fruit phytoliths are also less abundant in the eastern area, suggesting
454 that fruit and other plant foods were mainly processed in the western area.
455 Micromorphological samples 8 (square B5), 11, and 16 (C5), where bioturbation and diagenesis
456 are low and there is clear distinction between combustion products and substrate, can be
457 interpreted as hearths. In sample 16, the lower part of the thin section represents the intact
458 substrate or reddened clay on which combustion occurred, as indicated by the overlying bed
459 rich in phosphate ash, charcoal and burnt bone (Aldeias et al., 2016). The homogeneous
460 mixture of bone, charcoal, and phosphates on this surface, which shows no evidence of
461 bedding or horizontal fabric of the coarse components, may be interpreted as evidence of
462 sweeping or trampling of combustion debris (Goldberg et al., 2009).

463 4.2.3 Variable effects of recent disturbance

464 Different post-depositional processes affected the contexts, based on the occurrence of
465 pedofeatures. Almost all the micromorphological samples, except for 6, 7 (square A2), 8 (B5),
466 and 16 (C5), are affected by bioturbation by microfauna, as evidenced by channels filled with
467 churned up aggregates of silty clay. At least a small part of this activity was recent, based on
468 the presence of calcitic dung spherulites in some samples, especially near the contact with
469 Layer A, indicating disturbance by shepherd activities. Similarly, the fragments of land snail
470 shells in Layer A-associated samples 4 and 5 (square B2) appear to be the result of recent
471 faunal activity. These shells may represent the most recent episode of bioturbation, given the
472 presence of authigenic phosphates, which are likely to have formed under conditions in which
473 the calcium carbonate shells would have dissolved (Weiner, 2010).

474 The results confirm the archaeological observations suggesting that modern disturbance by
475 shepherds occurred mainly in the central area of the cave (in square B3, and the boundary
476 samples from squares A2, B2, B4 and B5) and in the sounding squares (F2, F3 and F4) affecting
477 Layers A and B. This disturbance is well-defined, confirming that neither the western nor the
478 eastern areas of the cave have been recently reworked. Therefore, the archaeological record
479 (micro and macro) recovered from this central area (mainly square B3) does not represent an *in*
480 *situ* EUP assemblage. The occurrence of transforming apatite at the boundary between
481 samples of square B4 and B5 indicates continuous postdepositional alteration, if not strong
482 diagenesis of the original ash, as suggested by the absence of leucophosphite (Weiner et al.,
483 2002).

484 4.3 Plants present at the site

485 The phytolith record in Layer B samples from MHM shows an overall low concentration of
486 phytoliths, which can have three possible explanations: i) dissolution, ii) the presence of non-
487 rich phytolith-producing plants and iii) the absence of plants. We discard the third possibility,
488 as charred seeds and charred wood remains have been widely identified in most of the
489 samples (White et al., 2019). Regarding phytolith dissolution, the phytolith record shows little
490 weathering. Phytoliths are well preserved at pH <8.2 (Cabanés et al., 2011), which seems to be
491 the case for the sedimentary context at MHM. Therefore, the overall low concentrations of
492 phytoliths must be explained by the diversity of plants present at the site, which are not
493 phytolith-rich producer plants. Dicots make up a significant proportion of the undisturbed
494 Layer B phytolith assemblage, including dicot fruit phytoliths. Both wood/bark, and dicot fruits
495 produce low amounts of phytoliths and, as a result, are usually underrepresented in the
496 phytolith record, particularly when compared to monocot plants (Albert & Weiner, 2001;
497 Tsartsidou et al., 2007). Poaceae phytoliths are the most abundant in the assemblage (mean
498 50.4%) (Fig. 11). The question is whether their presence is due to their use as tinder or as
499 contamination, as several studies show that they can be introduced as contamination by

500 adhering to the wood/bark of the dicots, between 30 and 49% in the Mediterranean area
501 (Albert et al., 2000; Tsartsidou et al., 2007) and up to 44% in South Africa (Esteban et al., 2017).
502 Considering that in our hearth-related samples (C2, C3 and C4) the percentage of Poaceae
503 phytoliths is between 54 and 64.7%, much higher than that observed when they appear as
504 contamination with the wood, we suggest that the presence of grasses in these burning
505 contexts could potentially be related to an intentional use of these plants, probably as tinder.

506 In square B2, where dicotyledonous phytoliths from wood/bark were more abundant, the FTIR
507 results indicated the presence of diagenetically altered calcitic ash, suggesting that they were
508 part of the fuel residues (ash) generated by combustion processes. The presence of siliceous
509 aggregates in and around the hearths, in samples from Layer B suggests ash dispersion (Table
510 3). Siliceous aggregates are quite stable and can persist after strong diagenetic processes have
511 occurred (Schiegl et al., 1996). However, the absence of ash-derived calcite in the same
512 samples indicates that calcite has undergone diagenesis, which also explains the absence of
513 ash pseudomorphs. Ash dispersion in cave deposits has been reported in Middle Palaeolithic
514 caves such as Kebara Cave (Israel) and Abrigo de la Quebrada (Spain) (Albert et al., 2000;
515 Esteban et al., 2015).

516 Dicots fruits could be anthropogenic or natural inputs (e.g., from bird or bat guano input when
517 humans were absent). No abrupt or sustained interruptions in the archaeological deposition
518 regime were identified within Layer B. This, together with the absence of carbonate
519 hydroxylapatite in the sediment makes it less probable that the dicots fruits came from bird or
520 bat droppings (Shahack-Gross et al., 2004). Another possible pathway is through the burning of
521 wood, as fruit trees were part of the local vegetation around the cave. This would involve
522 collecting either green branches with unripe fruit, or dry branches with some fruit still
523 attached, for use as fuel. Along with the presence of phytoliths from dicots fruit, charred seeds
524 from different edible plants from the Fabaceae (*Lens*, *Vicia* and *Lathyrus*), *Ficus*, and *Pistacia*
525 were recovered in Layer B flotation samples, especially from squares A2 and A1. Charred wood
526 from *Quercus* deciduous type, *Pistacia*, and *Amygdalus* were also recovered from these
527 samples (White et al., 2019). Wild legumes and pistachios are important, often dominant
528 components of macrobotanical assemblages from Late Pleistocene archaeological contexts in
529 southwest Asia (Lev et al., 2005; Kabukcu et al., 2021). With additional processing such as
530 heating or soaking to help remove antinutrients, wild legume seeds could have been used for
531 human consumption. Ongoing macrobotanical analyses and future microarchaeological
532 sampling will aim to resolve the question of whether fruits were gathered food resources.

533 The archaeobotanical data from MHM cave integrates well with preliminary microfaunal data
534 (Stutz et al., 2015), indicating that the site was in an ecotonal setting. At ca. 80 m asl, MHM
535 today is open, dominated by heavily grazed grasses and shrubs. Mediterranean forest prevails
536 to the east, with a transition to oak-dominated vegetation above 400-500 m asl, located several
537 kilometres upslope from MHM (which sits at ca. 80 m asl), toward the Transjordanian Plateau's
538 upland zone, dominated by oak and pine forest. Overall, the macrobotanical results from Layer
539 B at MHM point to a nearby landscape dominated by Mediterranean forest. As noted above,
540 preliminary results on identifications of carbonised seeds and nutshells (White et al., 2019)
541 emphasises the abundance of wild legumes and pistachio shell fragments. This is similar to the
542 results obtained in the late Mousterian context of Kebara Cave (ca. 65-50 ka BP) (Lev et al.,
543 2005; Weiss, 2017), located in the Mediterranean vegetation zone on southern Mt. Carmel.
544 Preliminary examination of wood charcoal from Layer B at MHM also indicates the presence of
545 hardwood species occurring in Mediterranean forest regimes (Stutz et al., 2016). From the
546 undisturbed Layer B phytolith assemblage, the major presence of Poaceae of the C₃ pooid
547 subfamily are indicative of a Mediterranean woodland biome, usually related to more forested
548 vegetation. Multiple lines of evidence point toward Mediterranean woodland substantially

549 closer to the site than is the case today (Stutz and Nilsson Stutz, 2017). Ongoing wood-charcoal
550 analyses and light stable isotope analyses of ungulate tooth enamel may yield more precise
551 vegetation-band reconstructions. A plausible expectation is that, with MIS 3 conditions
552 generally cooler than the present climate, meso-mediterranean vegetation may have extended
553 toward MHM's elevation, at ca. 80 m asl, with supra-mediterranean forest vegetation within a
554 few kilometer's walk uphill. At the same time, the identification of C₄ plant suggest the
555 presence of xerophilic plants, more related to arid environments. On the other hand, in the
556 Jordan Valley palms are related to well-water areas (Bremond et al., 2008), which is consistent
557 with localized wetland environments around springs and seeps at lower elevations, as well as
558 the proximity of the Lake Lisan.

559 **Conclusions**

560 The multi-proxy approach presented here has allowed the identification of different post-
561 depositional processes affecting different areas of the EUP deposits represented by Layer B in
562 the MHM cave. First, modern shepherd disturbance has thoroughly affected the central area of
563 the cave, leading to the formation of Layer A, especially in square B3 and partially the adjacent
564 squares (A1, A2, B2, B4, and B5). Except for parts of square B5, where microfaunal activity has
565 mixed traces of modern dung with Layer B sediments, the eastern and western areas close to
566 the walls of the cave do not show modern disturbance impacts. The archaeological
567 assemblages recovered from these areas represent undisturbed EUP activity areas. Conversely,
568 in the western area of the cave, diagenesis has affected bone preservation, but not that of
569 phytoliths and charred plant macro-remains. The presence of C₃ and C₄ phytoliths in
570 association with other macrobotanical remains indicates that, during the EUP occupation of
571 MHM, wetter areas and Mediterranean woodland vegetation were located near the site, while
572 arid-adapted grasses are also present. The presence of dicot phytoliths and charcoal indicates
573 their use as fuel, alongside grasses, which might be used as tinder. In addition, the presence of
574 siliceous aggregates in and around the hearths suggests ash dispersion. Finally, the
575 concentration of fruit phytoliths, probably of anthropogenic origin, in the western area
576 complements the macrobotanical remains of edible seeds and suggest the incorporation of
577 such plant resources into the diet.

578 **Authors contribution**

579 **Mónica Alonso-Eguiluz:** Conceptualization, Formal analysis, Investigation, Writing–original
580 draft, Visualization, Writing–review & editing. **Michael B. Toffolo:** Formal analysis,
581 Investigation, Writing–original draft, Visualization, Writing–review & editing. **Chantel E. White:**
582 Writing–review & editing. **Eleni Asouti:** Writing–review & editing. **Elisabetta Boaretto:** Writing–
583 review & editing. **Aaron Stutz:** Project administration, Funding acquisition, Resources,
584 Supervision, Writing–review & editing. **Liv Nilsson Stutz:** Project administration, Funding
585 acquisition, Supervision, Writing–review & editing. **Rosa María Albert:** Conceptualization,
586 Resources, Project administration, Funding acquisition, Supervision, Writing–review & editing.

587 **Acknowledgments**

588 The excavations and research on of MHM have been supported by Oxford College of Emory
589 University; a Gregory-Rackley Career Development Award to A. J. Stutz; NSF High Risk Research
590 in Anthropology Grant (#1025352); the L. S. B. Leakey Foundation; the Wenner-Gren
591 Foundation for Anthropological Research; the MICRO-PAST project funded by the Spanish
592 Ministry of Science and Innovation to RMA (PID2020-119773GB-100); 65 backers of the
593 crowdfunded project, “How Did Palaeolithic Hunter-Gatherers Use and Consume Plant
594 Resources in Eurasia” on Experiment (<https://doi.org/10.18258/9109>); the Irene Lévi-Sala CARE
595 Foundation; and the American Philosophical Society. We are grateful to the Department of

596 Antiquities of Jordan. MBT is supported by the grant RYC2021-030917-I, funded by
597 MCIN/AEI/10.13039/501100011033 and by the “European Union NextGenerationEU/PRTR”,
598 and wishes to thank Archéosciences Bordeaux for the possibility to use the petrographic
599 microscope to study thin sections at an earlier stage.

600 **References**

- 601 Albert, R.M., Weiner, S., 2001. Study of phytoliths in prehistoric ash layers from Kebara and
602 Tabun caves using a quantitative approach., in: Meunier, J.D., Colin, F., Faure-Denard, L. (Eds.),
603 Phytoliths, Applications in Earth Science and Human History. Lisse: Balkema, pp. 251–266.
- 604 Albert, R.M., Bamford, M.K., Cabanes, D., 2009. Palaeoecological significance of palms at
605 Olduvai Gorge, Tanzania, based on phytolith remains. *Quaternary International*, 193(1–2), 41–
606 48. <https://doi.org/10.1016/j.quaint.2007.06.008>
- 607 Albert, R.M., Berna, F., Goldberg, P., 2012. Insights on Neanderthal fire use at Kebara Cave
608 (Israel) through high resolution study of prehistoric combustion features: Evidence from
609 phytoliths and thin sections. *Quaternary International* 247, 278-293.
610 <https://doi.org/10.1016/j.quaint.2010.10.016>
- 611 Albert, R.M., Weiner, S., Bar-Yosef, O., Meignen, L., 2000. Phytoliths in the Middle Palaeolithic
612 deposits of Kebara Cave, Mt Carmel, Israel: Study of the plant materials used for fuel and other
613 purposes. *J. Archaeol. Sci.*, 27(10), 931–947. <https://doi.org/10.1006/jasc.2000.0507>
- 614 Aldeias, V., Dibble, H.L., Sandgath, D., Goldberg, P., McPherron, S.J.P., 2016. How heat alters
615 underlying deposits and implications for archaeological fire features: A controlled experiment.
616 *J. Archaeol. Sci.* 67, 64-79. <https://doi.org/10.1016/j.jas.2016.01.016>
- 617 Berna, F., Behar, A., Shahack-Gross, R., Berg, J., Boaretto, E., Gilboa, A., Sharon, I., Shalev, S.,
618 Shilstein, S., Yahalom-Mack, N., Zorn, J.R., Weiner, S., 2007. Sediments exposed to high
619 temperatures: reconstructing pyrotechnological processes in Late Bronze and Iron Age Strata at
620 Tel Dor (Israel). *J. Archaeol. Sci.* 34, 358–373. <https://doi.org/10.1016/j.jas.2006.05.011>
- 621 Berna, F., Boaretto, E., Wiebe, M.C., Goder-Goldberger, M., Abulafia, T., Lavi, R., Barzilai, O.,
622 Marder, O., Weiner, S., 2021. Site formation processes at Manot Cave, Israel: Interplay between
623 strata accumulation in the occupation area and the talus. *Journal of Human Evolution* 160,
624 102883. <https://doi.org/10.1016/j.jhevol.2020.102883>
- 625 Blinnikov, M.S., 2005. Phytoliths in plants and soils of the interior Pacific Northwest, USA. *Rev.*
626 *Palaeobot. Palynol.* 135, 71–98. <https://doi.org/10.1016/j.revpalbo.2005.02.006>
- 627 Bremond, L., Alexandre, A., Wooller, M. J., Hély, C., Williamson, D., Schäfer, P. A., Majule, A.,
628 Guiot, J., 2008. Phytolith indices as proxies of grass subfamilies on East African tropical
629 mountains. *Global and Planetary Change*, 61(3–4), 209–224.
630 <https://doi.org/10.1016/j.gloplacha.2007.08.016>
- 631 Cabanes, D., Weiner, S., Shahack-Gross, R. 2011. Stability of phytoliths in the archaeological
632 record: a dissolution study of modern and fossil phytoliths. *J. Archaeol. Sci.* 38, 2480–2490.
633 <https://doi.org/10.1016/j.jas.2011.05.020>
- 634 Chauhan, D.K., Tripathi, D.K., Kumar, D., Kumar, Y., 2011. Diversity, distribution, and frequency-
635 based attributes of phytolith in *Arundo donax* L. *International Journal of Innovations in*
636 *Biological and Chemical Sciences* 1, 22–27.

- 637 Durn, G., Ćorić, R., Tadej, N., Barudžija, U., Rubinić, V., Husnjak, S. 2014. Bulk and clay mineral
638 composition indicate origin of terra rossa soils in Western Herzegovina. *Geol. Croat.* 67, 171–
639 183. <https://doi.org/10.4154/gc.2014.13>
- 640 Esteban, I., Albert, R.M., Eixea, A., Zilhão, J., Villaverde, V. 2015. Neanderthal use of plants and
641 past vegetation reconstruction at the Middle Paleolithic site of Abrigo de la Quebrada (Chelva,
642 Valencia, Spain). *Archaeological and Anthropological Sciences*, 9(2), 265–278.
643 <https://doi.org/10.1007/s12520-015-0279-7>
- 644 Esteban, I., Vlok, J., Kotina, E.L., Bamford, M.K., Cowling, R.M., Cabanes, D., Albert, R.M. 2017.
645 Phytoliths in plants from the south coast of the Greater Cape Floristic Region (South Africa).
646 *Rev. Palaeobot. Palynol.* 245, 69–84. <https://doi.org/10.1016/j.revpalbo.2017.05.001>
- 647 Esteban, I., Bamford, M.K., House, A., Miller, C.S., Neumann, F.H., Schefuß, E., Pargeter, J.,
648 Cawthra, H.C., Fisher, E.C., 2020. Coastal palaeoenvironments and hunter-gatherer plant-use at
649 Waterfall Bluff rock shelter in Mpondoland (South Africa) from MIS 3 to the Early Holocene.
650 *Quaternary Science Reviews*, 250, 106664. <https://doi.org/10.1016/j.quascirev.2020.106664>
- 651 Flügel, E. 2004. *Microfacies of carbonate rocks: Analysis, interpretation and application.*
652 Springer, Berlin
- 653 Fredlund, G.G., Tieszen, L.T., 1994. Modern Phytolith Assemblages from the North American
654 Great Plains. *J Biogeogr* 21, 321–335. <https://doi.org/10.2307/2845533>
- 655 Goldberg, P., Berna, F., Chazan, M., 2015. Deposition and Diagenesis in the Earlier Stone Age of
656 Wonderwerk Cave, Excavation 1, South Africa. *African Archaeological Review* 32, 613–643.
657 <https://doi.org/10.1007/s10437-015-9192-9>
- 658 Goldberg, P., Miller, C.E., Schiegl, S., Ligouis, B., Berna, F., Conard, N.J., Wadley, L. 2009.
659 Bedding, hearths and site maintenance in the Middle Stone Age of Sibudu Cave, KwaZulu-Natal,
660 South Africa. *Archaeological and Anthropological Sciences* 1, 95–122.
661 <https://doi.org/10.1007/s12520-009-0008-1>
- 662 Gur-Arieh, S., Mintz, E., Boaretto, E., Shahack-Gross, R., 2013. An ethnoarchaeological study of
663 cooking installations in rural Uzbekistan: development of a new method for identification of
664 fuel sources. *J. Archaeol. Sci.* 40, 4331–4347. <https://doi.org/10.1016/j.jas.2013.06.001>
- 665 Kabukcu, C., Asouti, E., Pöllath, N., Peters, J., Karul, N., 2021. Pathways to plant domestication
666 in Southeast Anatolia based on new data from aceramic Neolithic Gusir Höyük. *Scientific*
667 *Reports* 11, 2112. <https://doi.org/10.1038/s41598-021-81757-9>
- 668 Karkanas, P., Bar-Yosef, O., Goldberg, P., Weiner, S., 2000. Diagenesis in Prehistoric Caves: the
669 Use of Minerals that Form In Situ to Assess the Completeness of the Archaeological Record.
670 *Journal of Archaeological Science* 27, 915–929. <https://doi.org/10.1006/jasc.1999.0506>
- 671 Karkanas, P., Rigaud, J.-P., Simek, J.F., Albert, R.M., Weiner, S., 2002. Ash bones and guano: a
672 study of the minerals and phytoliths in the sediments of Grotte XVI, Dordogne, France. *J.*
673 *Archaeol. Sci.* 29, 721–732. <https://doi.org/10.1006/jasc.2001.0742>
- 674 Katz, O., Cabanes, D., Weiner, S., Maeir, A.M., Boaretto, E., Shahack-Gross, R., 2010. Rapid
675 phytolith extraction for analysis of phytolith concentrations and assemblages during an
676 excavation: an application at Tell es-Safi/Gath, Israel. *J. Archaeol. Sci.* 37, 1557–1563.
677 <https://doi.org/10.1016/j.jas.2010.01.016>
- 678 Kadowaki, S., Tamura, T., Kida, R., Omori, T., Maher, L. A., Portillo, M., Hirose, M., Suga, E.,
679 Massadeh, S., Henry, D. O. (2021). *Lithic Technology and Chronology of Initial Upper Paleolithic*

- 680 Assemblages at Tor Fawaz, Southern Jordan. *Journal of Paleolithic Archaeology*, 5(1).
681 <https://doi.org/10.1007/s41982-021-00107-3>
- 682 Kehl, M., Burow, C., Cantalejo, P., Domínguez-Bella, S., Durán, J. J., Henselowsky, F., Klasen, N.,
683 Linstädter, J., Medianero, J., Pastoors, A., Ramos, J., Reicherter, K., Schmidt, C., Weniger, G. C.
684 (2016). Site formation and chronology of the new Paleolithic site Sima de Las Palomas de Teba,
685 southern Spain. *Quaternary Research*, 85(2), 313-331.
686 <http://dx.doi.org/10.1016/j.yqres.2016.01.007>
- 687 Lev, E., Kislev, M.E., Bar-Yosef O., 2005. Mousterian vegetal food in Kebara Cave, Mt. Carmel. *J.*
688 *Archaeol. Sci.* 32, 475–484. <https://doi.org/10.1016/j.jas.2004.11.006>
- 689 Macphail, R.I., Goldberg, P., 2017. *Applied Soils and Micromorphology in Archaeology*.
690 Cambridge University Press, Cambridge.
- 691 Mercier, N., Valladas, H., Joron, J.L., Schiegl, S., Bar Yosef, O., Weiner, S., 1995.
692 Thermoluminescence Dating and the Problem of Geochemical Evolution of Sediments – A Case
693 Study: The Mousterian Levels at Hayonim. *Israel Journal of Chemistry* 35, 137-141.
694 <https://doi.org/10.1002/ijch.199500021>
- 695 Mulholland, S.C., Rapp, G., 1992. A Morphological Classification of Grass Silica-Bodies. *Phytolith*
696 *Systematics* 65–89. https://doi.org/10.1007/978-1-4899-1155-1_4
- 697 Neumann, K., Strömberg, C.A.E., Ball, T., Albert, R.M., Vrydaghs, L., Cummings, L.S., 2019.
698 International Code for Phytolith Nomenclature (ICPN) 2.0. *Ann Bot* XX, 1–11.
699 <https://doi.org/10.1093/aob/mci172>
- 700 Nicosia, C., Stoops, G., 2017. *Archaeological Soil and Sediment Micromorphology*. Wiley
701 Blackwell.
- 702 Piperno, D., 2006. *Phytoliths. A comprehensive guide for archaeologists and paleoecologists*.
703 Altamira Press.
- 704 Regev, L., Poduska, K.M., Addadi, L., Weiner, S., Boaretto, E., 2010. Distinguishing between
705 calcites formed by different mechanisms using infrared spectrometry: archaeological
706 applications. *J. Archaeol. Sci.* 37, 3022–3029. <https://doi.org/10.1016/j.jas.2010.06.027>
- 707 Reimer, P., Austin, W., Bard, E., Bayliss, A., Blackwell, P., Bronk Ramsey, C., Butzin, M., Cheng, H.,
708 Edwards, R., Friedrich, M., Grootes, P., Guilderson, T., Hajdas, I., Heaton, T., Hogg, A., Hughen,
709 K., Kromer, B., Manning, S., Muscheler, R., Palmer, J., Pearson, C., van der Plicht, J., Reimer, R.,
710 Richards, D., Scott, E., Southon, J., Turney, C., Wacker, L., Adolphi, F., Büntgen, U., Capano, M.,
711 Fahrni, S., Fogtmann-Schulz, A., Friedrich, R., Köhler, P., Kudsk, S., Miyake, F., Olsen, J., Reinig, F.,
712 Sakamoto, M., Sookdeo, A., Talamo, S., 2020. The IntCal20 Northern Hemisphere radiocarbon
713 age calibration curve (0–55 cal kBP). *Radiocarbon*, 62.
- 714 Rodríguez-Cintas, A., Albert, R.M., Bamford, M.K., Stanistreet, I.G., Stollhofen, H., Stone, J.R.,
715 Rivera-Rondón, C., Pronzato, R., Njau, J.K., Schick, K., Toth, N., 2020. Palaeovegetation changes
716 recorded in Palaeolake Olduvai OGCP Core 2A (2.09–2.12 Ma) Naibor Soit Formation Olduvai
717 Gorge, Tanzania. *Palaeogeogr. Palaeoclimatol. Palaeoecol.* 557.
718 <https://doi.org/10.1016/j.palaeo.2020.109928>
- 719 Runge, F. 1999. The opal phytolith inventory of soils in central Africa — quantities, shapes,
720 classification, and spectra. *Rev. Palaeobot. Palynol.* 107, 23–53.

- 721 Schiegl, S., Goldberg, P, Bar-Yosef O, Weiner S (1996) Ash deposits in Hayonim and Kebara
722 Caves, Israel: Macroscopic, microscopic and mineralogical observations, and their
723 archaeological implications. *J. Archaeol. Sci.* 23, 763–781.
724 <https://doi.org/10.1006/jasc.1996.0071>
- 725 Shahack-Gross, R. 2011. Herbivorous livestock dung: formation, taphonomy, methods for
726 identification, and archaeological significance. *J. Archaeol. Sci.* 38, 205–218.
727 <https://doi.org/10.1016/j.jas.2010.09.019>
- 728 Shahack-Gross, R., Albert, R.M., Gilboa, A., Nagar-Hilman, O., Sharon, I., Weiner, S., 2005.
729 Geoarchaeology in an urban context: The uses of space in a Phoenician monumental building
730 at Tel Dor (Israel). *J. Archaeol. Sci.* 32, 1417–1431. <https://doi.org/10.1016/j.jas.2005.04.001>
- 731 Shahack-Gross, R., Berna, F., Karkanas, P., Weiner, S., 2004. Bat guano and preservation of
732 archaeological remains in cave sites. *Journal of Archaeological Science* 31, 1259-1272.
733 <https://doi.org/10.1016/j.jas.2004.02.004>
- 734 Shakoor, S.A., Soodan, A.S., Kumar, K., 2014. Morphological Diversity and Frequency of
735 Phytolith Types in Gaint Reed *Arundo donax* (L.). *World Appl. Sci. J.* 29, 926–932.
736 <https://doi.org/10.5829/idosi.wasj.2014.29.07.14>
- 737 Shea, J.J., Stutz, A.J., Nilsson Stutz, L., 2019. An Early Upper Palaeolithic Stone Tool Assemblage
738 from Mughr El-Hamamah, Jordan: An Interim Report. *J. F. Archaeol.* 44, 420–439.
739 <https://doi.org/10.1080/00934690.2019.1655519>
- 740 Stoops, G., Marcelino, V., Mees, F., 2018. Interpretation of Micromorphological Features of
741 Soils and Regoliths, Second ed. Elsevier, Oxford.
- 742 Stoops, G., 2021. Guidelines for Analysis and Description of Soil and Regolith Thin Sections,
743 Second ed. Wiley.
- 744 Stutz, A.J., Shea, J.J., Rech, J. A., Pigati, J.S., Wilson, J., Belmaker, M., Albert, R.M., Arpin, T.,
745 Cabanes, D., Clark, J.L., Hartman, G., Hourani, F., White, C.E., Nilsson Stutz, L. 2015. Early Upper
746 Paleolithic chronology in the Levant: new ABOx-SC accelerator mass spectrometry results from
747 the Mughr el-Hamamah Site, Jordan. *J. Hum. Evol.* 85, 157–173.
748 <https://doi.org/10.1016/j.jhevol.2015.04.008>
- 749 Stutz, A.J., Albert, R.M., Alonso-Eguiluz, M., Arpin, T., Asouti, E., White, C.E., Shea, J.J., Nilsson
750 Stutz, L.G., 2016. Depositional Context of the Early Upper Paleolithic Occupation (45–39 ka) at
751 Mughr el-Hamamah, Jordan: Implications for Tracing Behavioral Change across the Middle-
752 Upper Paleolithic Transition. Presented at the Paleoanthropology Society Annual Meeting,
753 Atlanta.
- 754 Stutz, A. J., Nilsson Stutz, L. 2017. Mughr el-Hamamah: An Early Upper Palaeolithic Cave Site on
755 the Eastern Jordan Valley Flanks. *Quaternary of the Levant: Environments, Climate Change, and*
756 *Humans*, 285–290.
- 757 Taifour, H., El-Oqlah, A., 2016. The plants of Jordan. An annotated checklist, *Raffles Bulletin of*
758 *Zoology Supplement*. Key Publishing. Royal Botanic Garden.
- 759 Toffolo, M. B., Brink, J. S., van Huyssteen, C., Berna, F., 2017. A microstratigraphic reevaluation
760 of the Florisbad spring site, Free State Province (South Africa): formation processes and
761 paleoenvironment. *Geoarchaeology* 32 (4), 456-478. <https://doi.org/10.1002/gea.21616>
- 762 Tsartsidou, G., Lev-Yadun, S., Albert, R.M., Miller-Rosen, A., Efstratiou, N., Weiner, S., 2007. The
763 phytolith archaeological record: strengths and weaknesses evaluated based on a quantitative

- 764 modern reference collection from Greece. *J. Archaeol. Sci.* 34, 1262–1275.
765 <https://doi.org/10.1016/j.jas.2006.10.017>
- 766 Twiss, P.C., 1992. Predicted world distribution of C3 and C4 grass phytoliths, in: Rapp, G.,
767 Mulholland, S.C. (eds). *Phytolith Systematics. Emerging Issues. Advances in Archaeological and*
768 *Museum Science.* pp. 113–128.
- 769 Vepraskas, M.J., Lindbo, D.L., Stolt, M.H., 2018. Redoximorphic Features. In: Stoops, G.,
770 Marcelino, V., Mees, F. (eds) *Interpretation of Micromorphological Features of Soils and*
771 *Regoliths, Second ed.* Elsevier, Oxford, pp 425-446.
- 772 Weiner, S., 2010. *Microarchaeology. Beyond the Visible Archaeological Record.* Cambridge
773 University Press, New York.
- 774 Weiner, S., Goldberg, P., Bar-Yosef, O., 1993. Bone preservation in Kebara Cave, Israel using on-
775 site fourier transform infrared spectrometry. *J. Archaeol. Sci.* 20, 613–627.
776 <https://doi.org/10.1006/jasc.1993.1037>
- 777 Weiner, S., Goldberg, P., Bar-Yosef, O., 2002. Three-dimensional distribution of minerals in the
778 sediments of Hayonim Cave, Israel: Diagenetic processes and archaeological implications. *J.*
779 *Archaeol. Sci.* 29, 1289–1308. <https://doi.org/10.1006/jasc.2001.0790>
- 780 Weiner, S., Berna, F., Cohen, I., Shahack-Gross, R., Albert, R.M., Karkanas, P., Meignen, L., Bar-
781 Yosef, O., 2007. Mineral distributions in Kebara Cave: diagenesis and its effect on the
782 archaeological record, in: Bar-Yosef, O., Meignen, L. (Eds.), *Kebara Cave, Mt. Carmel, Israel: The*
783 *Middle and Upper Paleolithic Archaeology, Part 1.* Peabody Museum of Archaeology and
784 Ethnology, Harvard University, Cambridge, MA, pp. 131-146.
- 785 Weiss, E., 2017, "Palaeolithic Vegetal Diet in the Southern Levant", in O. Bar-Yosef y Y., Enzel
786 (eds.), *Quaternary of the Levant: Environments, Climate Change, and Humans.* Cambridge, pp.
787 329-336. <https://doi.org/10.1017/9781316106754.038>
- 788 White, C., McKain, K., Nilsson Stutz, L., Stutz, A., Asouti, E., 2019. A New Assessment of
789 Macrobotanical Preservation and Recovery: Results from the Early Upper Paleolithic Site of
790 Mughr el-Hamamah, Jordan. American Society of Overseas Research Annual Meeting, San
791 Diego.